

21

FLOWGO 2012: An Updated Framework for Thermorheological Simulations of Channel-Contained Lava

Andrew J. L. Harris¹ and Scott K. Rowland²

ABSTRACT

A new version of the thermo-rheological lava flow model FLOWGO allows (i) incorporation of new rheological relations, (ii) use of stochastic lava flow path models, and (iii) greater flexibility to allow best-fitting of model output with natural data. We apply the model to four channel-fed lava flows for which good field data exist. These include Mauna Loa's 1859 and 1984 flows plus Kīlauea's December 1974 flow. Best fits between model output and field data require (i) selection of an appropriate viscosity and crystallization model, (ii) a thermal model that moves from poorly insulated across proximal channel reaches to well insulated in medial-to-distal reaches, and (iii) a lava flow emplacement event that is cooling limited, not volume limited. For Mauna Loa's 1859 flow, if we use a thermal regime that changes from poorly insulated to well insulated at 10 km, we can re-create a transition between rapid and slow cooling witnessed at this point. For Kīlauea's 1974 flow, we model an appropriate thermal regime (i.e., cooling rates of 1.2°C/km). However, when fed at the actual effusion rate of at least 270 m³/s, the model gives a flow run out that is too long. A reasonable explanation is that this flow was volume limited.

21.1. INTRODUCTION

Lava flow emplacement modeling serves two purposes. First, models allow better understanding of the physical processes governing lava flow dynamics and emplacement as well as the complex feedbacks between cooling, crystallization, and rheology that govern flow dynamics [e.g., Daneš 1972; Park and Iverson, 1984; Dragoni, 1989; Heslop *et al.*, 1989; Crisp and Baloga, 1994; Keszthelyi and Self, 1998]. Second, models can be used to assess the likely lava flow path, run-out and inundation area for hazard assessment [e.g., Young and Wadge, 1990; Ishihara *et al.*, 1990; Crisci *et al.*, 2004; Hidaka *et al.*, 2005; Favalli *et al.*, 2005; Vicari *et al.*, 2007]. In addition, such simulations now have the potential to be run in real time using

satellite and/or field-derived lava discharge rates as input [Wright *et al.*, 2008; Herault *et al.*, 2009; Vicari *et al.*, 2009, 2011; Ganci *et al.*, 2012].

The FLOWGO model of Harris and Rowland [2001] was originally intended for the first purpose, as framework within which we could organize the complex links and feedbacks governing the thermal and rheological evolution of a lava control volume moving down a channel. It was designed to be highly flexible, so that thermal and rheological relationships could be modified and updated as our understanding and constraint of such relations evolved. It was also designed to be adaptive, so that input parameters could be set on a case-by-case basis so as to be tailored to the compositional, rheological, or thermal conditions appropriate to the flow in question [e.g., Rowland *et al.*, 2004; Mueller, 2005; Harris *et al.*, 2007; Riker *et al.*, 2009]. However, we found that the cooling-limited distance that the control volume could reach before freezing provided a reasonable approximation for actual channel length [Harris and

¹Laboratoire Magmas et Volcans, Université Blaise Pascal, Clermont Ferrand, France

²Department of Geology and Geophysics, University of Hawai'i at Mānoa, Honolulu, Hawaii, USA

Rowland, 2001]. Thus, FLOWGO has also been used to assess the likely distance a channel-fed flow can extend at a given rate of volumetric lava supply (i.e., effusion rate) and to assess the likely inundation hazard posed by emplacement of channel-fed lava flows [Rowland *et al.*, 2005; Harris *et al.*, 2011].

Since the initial presentation of FLOWGO by Harris and Rowland [2001], the code and its application have evolved significantly. We here present the latest version of FLOWGO (FLOWGO^s) that allows input and storage of a digital elevation model (DEM) and geolocated satellite-derived land cover map. This is used for projection of flow paths over the DEM, with a lava flow run-out model allowing estimation of the length down each flow path that a lava will likely extend. The reporting system then outputs results in map and table form, with simulations being projected over the satellite-derived base map [Harris *et al.*, 2011]. To achieve this, we have updated, combined, and tested two existing lava flow emplacement models: FLOWGO and the DOWN-FLOW model of Favalli *et al.* [2005]. DOWN-FLOW is used to yield flow paths, and FLOWGO estimates how far down each path a control volume will extend under given thermo-rheological and effusion rate conditions. Together, the two models provide a framework that allows us to explore our current understanding of thermo-rheological relations for active lavas.

21.2. PHYSICAL BASIS OF FLOWGO PROGRAM

The FLOWGO model tracks a control volume of lava as it moves down a channel of known starting dimensions. As the control volume is advanced down-channel, all heat losses and gains are calculated to determine the internal temperature and crystallinity of the control volume. These parameters, in turn, are used to calculate the viscosity and yield strength of the flow. These thermal, textural and rheological conditions are used to assess whether the lava is still capable of forward motion. The three stopping conditions can be summarized by the three following questions: Is the calculated velocity greater than zero? Is the temperature at or below the solidus? Is the yield strength at the base of the channel greater than the downhill stress? If none of these conditions are met, then advance of the control volume down-channel is continued. If any of the conditions is met, then the loop ends (Figure 21.1).

Velocity is therefore fundamental to the model as it determines whether the control volume is in motion or not. Mean velocity (v_{mean}) for a Newtonian fluid flowing in a channel can be calculated following Jeffreys [1925],

$$v_{\text{mean}} = \left(\frac{r^2 \rho g \sin(\theta)}{4\eta} \right), \quad (21.1a)$$

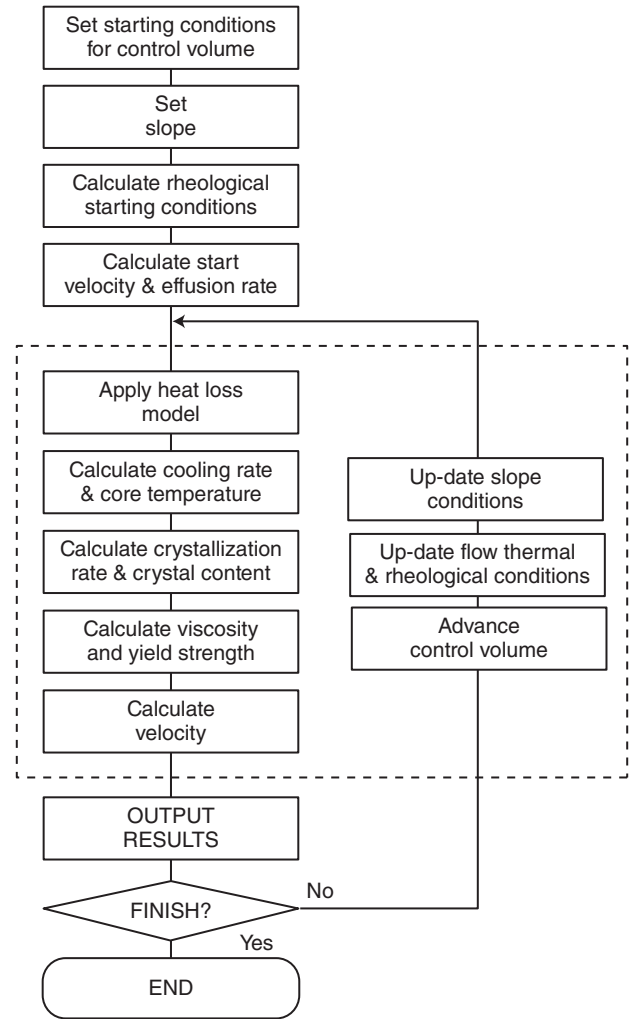


Figure 21.1 Flow chart giving the main steps executed by FLOWGO.

in which r is channel radius, ρ is lava density, g is acceleration due to gravity, θ is the underlying slope, n is a constant that depends on channel shape, and η is lava viscosity. However, the equation needs to be modified for a Bingham fluid so that, for a semicircular channel, we have [Moore, 1987]

$$v_{\text{mean}} = \left(\frac{r^2 \rho g \sin(\theta)}{8\eta} \right) \left[1 - \frac{4}{3} \frac{\tau_0}{\tau} + \frac{1}{3} \left(\frac{\tau_0}{\tau} \right)^4 \right] \quad (21.1b)$$

and for a channel that is wider than it is deep,

$$v_{\text{mean}} = \left(\frac{d^2 \rho g \sin(\theta)}{3\eta} \right) \left[1 - \frac{3}{2} \frac{\tau_0}{\tau} + \frac{1}{2} \left(\frac{\tau_0}{\tau} \right)^3 \right], \quad (21.1c)$$

where d is channel depth. The right-hand term takes into account Bingham conditions using the ratio of the lava

yield strength (τ_0) to the basal shear stress (τ). Note that when $\tau_0 = 0$ (i.e., the flow is Newtonian), the entire right-hand term reduces to 1. Basal shear stress is given by [Hulme, 1974]

$$\tau = d\rho g \sin(\theta), \quad (21.2)$$

in which d is lava thickness, which in our case equates to the depth of the lava in the channel.

Appropriate starting conditions (i.e., at-vent parameters for all values in equation (21.1)) are given for Mauna Loa's 1984 channel in Table 21.1 and for a channel active on Mount Etna during September 2004 in Table 21.2. To set up these starting conditions, density has been calculated from lava chemistry following the method of Bottinga and Weill [1970]. This dense rock value (ρ_{DRE}) needs to be corrected for vesicularity (ϕ_b) to derive a bulk density using

$$\rho = (1 - \phi_b) \rho_{\text{DRE}}, \quad (21.3)$$

ρ being the bulk density of the lava flowing in the channel.

Next, at-vent viscosity needs to be calculated. This can be obtained by applying models for fluid viscosity (η_f) for lava of given compositions and temperatures following the method of Shaw [1972] for Mauna Loa and Giordano and Dingwell [2003] for Etna. Bulk viscosity (η) has then, traditionally, been calculated using the fluid viscosity and lava crystal content from the Einstein-Roscoe relationship [e.g., Crisp *et al.*, 1994]. Likewise, yield strength can be calculated on the basis of temperature and crystal content, as shown in Tables 21.1 and 21.2.

The remaining at-vent variables in equation (21.1) are slope and channel radius or depth (d). Given an estimate

Table 21.1 Mean starting conditions for lava in Mauna Loa's 1984 channel and at-vent velocity and effusion rate that these give.

Parameter	Term	Value	Units	Source
Channel depth	r	3	m	Typical channel depth at 2850m vent outlet given in Table 57.3 of Lipman and Banks [1987]
Channel width	w	21	m	Typical channel width at 2850m vent outlet given in Table 57.3 of Lipman and Banks [1987]
Dense rock density	ρ_{DRE}	2720	kg/m	Density calculated from mean composition data given for Mauna Loa's 1984 lava by Rhodes [1988] using the method of Bottinga and Weill [1970]
Vesicularity	ϕ_b	32	%	Mean vesicularity calculated from bulk density data for channel samples given in Table 57.1 of Lipman and Banks [1987]
Bulk density	ρ	1850	kg/m ³	$\rho = (1 - \phi_b) \rho_{\text{DRE}}$
Slope	θ	2.7	deg	At-vent slope from DEM
Viscosity Model				
Fluid viscosity	$\eta_f(T)$	86	Pa·s	Viscosity calculated using the method of Shaw [1972] using the mean whole-rock composition for Mauna Loa's 1984 lava as given in Table 4 of Rhodes [1988] and an eruption temperature of 1140°C
Crystal content	ϕ	16.5	%	Median phenocryst content during 26 March to 6 April from data by Lipman and Banks [1987]
R	—	1.51	Dimensionless	Inverse of maximum crystal content
Bulk viscosity	η	177	Pa·s	$\eta(\phi) = \eta_f (1 - R\phi)^{-2.5}$
Yield Strength Model				
Eruption temperature	T_{erupt}	1140	°C	Mean from Lipman and Banks [1987]
Liquidus temperature	T_0	1120	°C	
Constant 1	B	0.01	Pa	From Dragoni [1989]
Constant 2	C	0.08	K ⁻¹	From Dragoni [1989]
Yield strength	τ_0	30	Pa	$\tau_0(T, \phi) = B \left[\exp^{C(T_0 - T_{\text{core}})} - 1 \right] + [6500 \phi^{2.85}]$
Basal shear stress	τ	4700	Pa	$\tau = d\rho g \sin(\theta)$
At-Vent (Starting) Velocity				
Mean velocity	V_{mean}	14.2	m/s	Equation (21.1c)
Effusion Rate				
Bulk effusion rate	E_r	893	m ³ /s	$E_r = d w v_{\text{mean}}$

Table 21.2 Mean starting conditions for lava in Etna's 2004 channel and at-vent velocity and effusion rate that these give.

Parameter		Value			Units	Source
Channel depth	r	1	1	1	m	Mean channel depth over first 100 m from Lidar data of <i>Mazzarini et al.</i> [2007]
Channel width	w	6	6	6	m	Mean channel width over first 100 m from Lidar data of <i>Mazzarini et al.</i> [2007]
Dense rock density	ρ_{DRE}	2,720	2,720	2,720	kg/m	Density calculated from composition data given for Etna's 1991–93 lavas by <i>Tonarini et al.</i> [1995] using the method of <i>Bottinga and Weill</i> [1970]
Vesicularity	ϕ_b	22	22	22	%	Mean vesicularity from Etna literature values collated by <i>Harris et al.</i> [2005]
Bulk density	ρ	2,120	2,120	2,120	kg/m	$\rho = (1 - \phi_b) \rho_{\text{DRE}}$
Slope	θ	29	29	29	deg	At-vent slope from LIDAR data of <i>Mazzarini et al.</i> [2007]
Viscosity Model						
Fluid Viscosity	$\eta_f(T)$	670	670	670	Pa·s	Method of <i>Giordano and Dingwell</i> [2003] applied using $\text{H}_2\text{O} = 0.1$ wt % and $T_{\text{erupt}} = 1065^\circ\text{C}$; H_2O content selected for Etna summit eruptions following <i>Harris and Allen</i> [2008]
Crystal content	ϕ	27	34	41	%	Mean phenocryst ($\pm 1\sigma$) content from all literature values for Etna collated by <i>Harris et al.</i> [2005]
R	—	1.51	1.51	1.51	Dimensionless	Inverse of maximum crystal content
Bulk viscosity	η	2,480	4,054	7,477	Pa·s	$\eta(\phi) = \eta_f (1 - R\phi)^{-2.5}$
Yield Strength Model						
Eruption temperature	T_{erupt}	1,065	1,065	1,065	$^\circ\text{C}$	At-vent internal temperature for lava channel active on Etna in 2001 [<i>Bailey et al.</i> , 2006]
Liquidus temperature	T_0	1,160	1,160	1,160	$^\circ\text{C}$	
Constant 1	B	0.01	0.01	0.01	Pa	From <i>Dragoni</i> [1989]
Constant 2	C	0.08	0.08	0.08	K^{-1}	From <i>Dragoni</i> [1989]
Yield strength	τ_0	163	308	519	Pa	$\tau_0(T, \phi) = B \left[\exp^{C(T_0 - T_{\text{core}})} - 1 \right] + \left[6500 \phi^{2.85} \right]$
Basal shear stress	τ	10,080	10,080	10,080	Pa	$\tau = d\rho g \sin(\theta)$
At-Vent (Starting) Velocity						
Mean velocity	V_{mean}	1.3	0.8	0.4	m/s	Equation (21.1c)
Effusion Rate						
Bulk effusion rate	E_r	8.0	4.7	2.2	m^3/s	$E_r = dwv_{\text{mean}}$

of at-vent channel depth and underlying slope, equation (21.1) can be solved to yield a mean velocity for lava at the head of the channel, as done in Tables 21.1 and 21.2. This now allows at-vent effusion rate (E_r) to be calculated from

$$E_r = dwv_{\text{mean}} \quad (21.4a)$$

which reduces to

$$E_r = d^2 v_{\text{mean}} \quad (21.4b)$$

for a square channel and

$$E_r = \pi d^2 v_{\text{mean}} \quad (21.4c)$$

for a semicircular channel.

In practice, a user may also have a measurement for E_r . Thus, a desired E_r can be input to the program and FLOWGO iterates equant (depth=width) at-vent channel dimensions until they, in combination with the underlying slope of the first 10 DEM pixels, yield the desired E_r . Beyond the first 10 DEM pixels, depth is held constant but width is allowed to vary so as to conserve volume (see below).

21.2.1. Down-flow Variation in Rheological Conditions

The main variables now controlling variations in flow velocity down the channel are slope, viscosity, and yield strength. These, in turn, can be linked to changes in lava internal temperature (T_{int}) and crystallinity (ϕ) through application of appropriate cooling and rheological models.

Viscosity can be defined for a mixture of liquid and solids (crystals) through the Einstein-Roscoe relationship whereby bulk viscosity can be defined as a function of crystallinity following [Einstein, 1906; Roscoe, 1952]

$$\eta(\phi) = \eta_f (1 - R\phi)^{-2.5} \quad (21.5)$$

in which η_f is the dynamic viscosity of the fluid and $R = 1/\phi_{\text{max}}$, ϕ_{max} being the maximum crystal content that the lava can attain before flow is rheologically impossible. In the original version of FLOWGO, η_f was calculated as a function of temperature (T) following [Dragoni, 1989]

$$\eta_f(T) = \eta_0 \exp^{A(T_0 - T_{\text{int}})}, \quad (21.6)$$

η_0 being dynamic viscosity at the liquidus temperature (T_0) and A is a constant. By inserting equation (21.6) into (21.5), bulk viscosity can be written as a function of temperature and crystallinity:

$$\eta(T, \phi) = \eta_f(T) (1 - R\phi)^{-2.5}, \quad (21.7a)$$

so that

$$\eta(T, \phi) = \eta_0 \exp^{A(T_0 - T_{\text{int}})} (1 - R\phi)^{-2.5} \quad (21.7b)$$

Likewise, yield strength can be written as a function of temperature and crystallinity following [Dragoni, 1989; Pinkerton and Stevenson, 1992]

$$\tau_0(T, \phi) = B \left[\exp^{C(T_0 - T_{\text{int}})} - 1 \right] + [6500 \phi^{2.85}]. \quad (21.8)$$

Now, given down-flow cooling and crystallization, viscosity and yield strength can be calculated as a function of flow internal temperature and crystal content.

These treatments ignore the effect of bubbles forming and deforming in the flowing lava. The bubble content may be more significant than the phenocryst content. For example, for the Mauna Loa 1984 lavas the at-vent phenocryst content was between 0 and 7% on the first day of the eruption, 25 March, increasing to 8%–15% during 26–28 March [Lipman and Banks, 1987]. In contrast, Lipman and Banks [1987] obtained maximum bubble contents of 85% and

described near-vent lava as “fluffy near–reticulite” with “the consistency of egg white”. The presence of bubbles in the lava mixture can increase the bulk viscosity if the bubbles are non-deformed and spherical or decrease the bulk viscosity if the bubbles are deformed and sheared [Manga *et al.*, 1998]. Hence, for mixtures of fluid and bubbles, Pal [2003] gives two forms of equation (21.5):

$$\eta(\phi_b) = \eta_f \left[1 - \frac{\phi_b}{\phi_{b,\text{max}}} \right]^{-\phi_{b,\text{max}}} \quad (21.9a)$$

for regimes in which the bubbles are spherical and

$$\eta(\phi_b) = \eta_f \left[1 - \frac{\phi_b}{\phi_{b,\text{max}}} \right]^{\frac{5\phi_{b,\text{max}}}{3}} \quad (21.9b)$$

in cases where the bubbles are sheared. Here, $\eta(\phi_b)$ is the viscosity of the fluid-bubble mixture, ϕ_b is the vesicularity, and $\phi_{b,\text{max}}$ is the maximum bubble content the mixture can attain before flow is rheologically impossible. If we set $\phi_{b,\text{max}}$ to unity, equations (21.9) and (21.10) reduce to [Llewellyn and Manga, 2005]:

$$\eta(\phi_b) = \eta_f [1 - \phi_b]^{-1} \quad (21.9c)$$

and

$$\eta(\phi_b) = \eta_f [1 - \phi_b]^{5/3} \quad (21.9d)$$

However, a lava will be a mixture of fluid, bubbles, and crystals. Hence a three-phase treatment is likely more appropriate. Phan-Thien and Pham [1997] introduced a treatment for the viscosity of a three-phase mixture comprising a suspension of rigid spheres and bubbles. They give three cases:

Case 1 Crystals smaller than bubbles:

$$\eta(\phi, \phi_b) = \eta_f \left[1 - \frac{\phi}{1 - \phi_b} \right]^{-5/2} (1 - \phi_b)^{-1}. \quad (21.10a)$$

Case 2 Crystals and bubbles of the same size range:

$$\eta(\phi, \phi_b) = \eta_f [1 - \phi - \phi_b]^{\frac{(5\phi - 2\phi_b)}{(2\phi - \phi_b)}}. \quad (21.10b)$$

Case 3 Crystals larger than bubbles:

$$\eta(\phi, \phi_b) = \eta_f \left[1 - \frac{\phi_b}{1 - \phi} \right]^{-1} (1 - \phi)^{-5/2}. \quad (21.10c)$$

When applied using chemical, temperature, crystallinity, and vesicularity data from Mauna Loa's 1984 lavas, results that are in excellent agreement with the velocity-based viscosity estimates of *Moore* [1987] are obtained [*Harris and Allen*, 2008].

21.2.2. Down-flow Variation in Thermal Conditions

To apply these rheological relationships, we need to estimate the down-flow evolution of the interior temperature and crystallinity of the lava flowing in the channel. Both rely on an estimate of down-flow cooling, which can be obtained by applying a heat budget model [e.g., *Danes*, 1972; *Park and Iversen*, 1984; *Crisp and Baloga*, 1994; *Keszthelyi and Self*, 1998]. The heat budget applied by FLOWGO incorporates heat lost by radiation, convection, conduction, and rain with heat gained due to heat of crystallization and viscous dissipation. These heat losses and gains, plus the budget that is rearranged next, is given in Table 21.3, with input constants and variables being defined in Table 21.4. The heat budget given in Table 21.3 can be rearranged to estimate cooling per unit distance ($\delta T/\delta x$) from

$$\frac{\delta T}{\delta x} = \frac{-Q_{\text{rad}} - Q_{\text{conv}} - Q_{\text{rain}} - Q_{\text{cond}} + Q_{\text{visc}}}{E_r \rho L (\delta \phi / \delta T)} \quad (21.11)$$

Heat loss due to entrainment of chilled surface crust can also be included within the model, as well as surface crust thickness, as detailed in Appendix A of *Harris and Rowland* [2001].

Cooling per unit distance is used to calculate the new internal temperature after the lava advances by the step distance. It can also be used to estimate the rate of crystallization per unit distance ($\delta \phi / \delta x$) from:

$$\frac{\delta \phi}{\delta x} = \frac{\delta T}{\delta x} \frac{\delta \phi}{\delta T}. \quad (21.12)$$

Crystallization rate is used to determine the new crystal content of the control volume once it has advanced by one step.

21.2.3. Volume Conservation and Stopping Conditions

FLOWGO conserves volume down-channel. That is, no volume is lost to the levees. Thus, the starting (vent-leaving) effusion rate is maintained down-channel. Given down-channel changes in velocity, the effusion rate must be maintained at each channel station by varying channel depth and/or width. We take a simple approach whereby flow depth is held constant at down-channel point x so that width varies as a function of velocity:

$$w(x) = E_r / v_{\text{mean}}(x), \quad (21.13)$$

where $v_{\text{mean}}(x)$ is the mean velocity calculated for channel station x and $w(x)$ is the channel width at the same station. Thus, as velocity declines, modeled channel width will increase, and vice versa.

Cooling and crystallization will eventually cause the viscosity and yield strength of the control volume to increase to a point where v_{mean} approaches zero. At this point, forward motion of the control volume stops. This point defines the cooling-limited distance the control volume will attain before freezing, that is, the distance a lava flow will move down a channel before cooling to a point at which additional motion is no longer possible. This point defines one of two potential stopping conditions of the FLOWGO loop. A second potential stopping condition occurs if the temperature of the control volume reaches the solidus of the particular lava composition that is input to the model. The value of the solidus temperature is independent of the FLOWGO model and must be input manually before running the program.

Table 21.3 Heat budget terms used in FLOWGO as modified from Table 3 of *Harris and Rowland* [2001].

Term	Definition	Derivation of flux in W/m
Q_{rad}	Radiative heat loss	$Q_{\text{rad}} = \sigma \epsilon [f T_{\text{crust}}^4 + (1-f) T_{\text{hot}}^4]^{0.25} w$
Q_{conv}	Convective heat loss (free or forced)	$Q_{\text{conv}} = h_c [f T_{\text{crust}}^{1.3} + (1-f) T_{\text{hot}}^{1.3}]^{0.75} w$
Q_{rain}	Heat loss due to rain vaporization	$Q_{\text{rain}} = \delta R / \delta t \rho_{\text{H}_2\text{O}} L_{\text{H}_2\text{O}} w$
Q_{cond}	Heat loss due to conduction through the flow base and levees	$Q_{\text{cond}} = \kappa_{\text{lava}} (\Delta T / \Delta h) w$
Q_{visc}	Heat from viscous dissipation	For a semi-circular channel: $Q_{\text{visc}} = \eta (v_{\text{mean}}/w)^2 d$ Where $w > d$ $Q_{\text{visc}} = \eta (v_{\text{mean}}/d)^2 w$
Q_{cryst}	Heat from crystallization	$Q_{\text{cryst}} = (\delta T / \delta x) E_r \rho L (\delta \phi / \delta T)$
$Q_{\text{in}} = Q_{\text{out}}$	Heat balance	$Q_{\text{rad}} + Q_{\text{conv}} + Q_{\text{rain}} + Q_{\text{cond}} = Q_{\text{visc}} + Q_{\text{cryst}}$ or $Q_{\text{rad}} + Q_{\text{conv}} + Q_{\text{rain}} + Q_{\text{cond}} = Q_{\text{visc}} + (\delta T / \delta x) E_r \rho L (\delta \phi / \delta T)$

Note: See Table 21.4 for definition of input parameters.

Table 21.4 Terms used for heat budget equations of Table 21.3.

Symbol	Definition	Units
d	Channel depth	m
f	Fractional crust cover	fraction
E_r	Effusion rate	m ³ /s
h_c	Convective heat transfer coefficient	W/mK
L	Latent heat of crystallization	J/kg
$L_{\text{H}_2\text{O}}$	Latent heat of vaporization plus heat required to heat water to 100°C	J/kg
T_{crust}	Crust (surface) temperature	K
T_{hot}	Hot crack temperature	K
v_{mean}	Mean velocity	m/s
w	Channel width	m
Δh	Height of thermal boundary layer at flow base	m
ΔT	Temperature difference across thermal boundary layer.	K
$\delta R/\delta t$	Rain fall rate	m/s
$\delta T/\delta x$	Cooling with distance	K/m
$\delta\phi/\delta T$	Crystallization per degree cooling	K ⁻¹
ϵ	Emissivity	
η	Lava viscosity	Pa · s
κ_{lava}	Thermal conductivity of lava	W/m · K
ρ	Lava bulk density	kg/m
$\rho_{\text{H}_2\text{O}}$	Water density	kg/m
σ	Stefan-Boltzmann constant	W/m · K

21.3. THERMAL AND VISCOSITY MODELS

FLOWGO provides a flexible framework within which thermal and rheological equations can be adjusted to assess the applicability of different thermo-rheological scenarios. The most effective way to achieve this is through adjustment of the thermal structure of the lava surface and/or the input viscosity to produce a best fit with available data.

21.3.1. Thermal Surface Model

Parameters that define the thermal surface from which heat is lost include (i) temperature of the surface crust (the cool component), (ii) temperature of lava exposed at cracks and across shear zones (the hot component), and (iii) fractional percentages of the cool and hot components (see Table 21.3). The better insulated (cooler and more heavily crusted) the surface, the lower the heat losses. Lower cooling rates mean that the control volume will extend farther before freezing, with increases in crystallization, viscosity, and yield strength being slower down-channel than in a high-cooling-rate (poorly insulated) case [Keszthelyi, 1995; Keszthelyi and Self, 1998]. Thus, crust cover percentage and crust and crack temperature are important model variables that control the distance the control volume will extend and the thermo-rheological changes that it will experience.

FLOWGO uses a two-component thermal surface whereby fraction f of the surface comprises a chilled crust at temperature T_{crust} , with the remainder $(1-f)$ of the surface comprising high-temperature zones at T_{hot} . The integrated temperature of that surface can be described by the effective radiation temperature (T_e) [Crisp and Baloga, 1994]:

$$T_e = [fT_{\text{crust}}^4 + (1-f)T_{\text{hot}}^4]^{1/4}, \quad (21.14)$$

Based on analysis of air photographs of the active 1984 Mauna Loa flow where velocity had been measured [Lipman and Banks, 1987], we developed an empirical relationship between crust growth and velocity:

$$f(V) = z \exp(yv_{\text{mean}}). \quad (21.15)$$

Harris and Rowland [2001] give $z=0.9$ and $y=-0.16$ for a poorly insulated flow and $z=1.0$ and $y=-0.00756$ for a more heavily crusted flow. Alternatively, crust cover can be set to be constant down-channel at a user-defined value between zero (crust free, poorly insulated) and unity (complete crust coverage, well insulated). Note that complete crustal coverage is not equivalent to flow in a lava tube [Rowland et al., 2005].

Similarly, crust temperature can be set to be constant or can be varied down-flow using a function whereby

crust temperature is related to time since it formed (t) following [Hon *et al.*, 1994]

$$T_{\text{crust}}(t) = m \log(t) + n. \quad (21.16)$$

Appropriate values for m and n for Hawaiian pāhoehoe are given by Hon *et al.* [1994] as -140 and 303 , with time being in units of hours and output temperature in degrees Celsius. Within the FLOWGO model, the time that a stable surface crust forming in the vent has had to cool can be calculated from the velocity of and distance traveled by the control volume. To achieve this, we calculate the time taken for the control volume to move across each step:

$$t_{\text{step}} = D_{\text{step}} / v_{\text{step}}, \quad (21.17)$$

where D_{step} is the step distance and v_{step} the mean velocity for that step. Summing these values for each step between

the vent and down-flow point x gives the travel time for the control volume between the vent and position x (i.e., t for use in equation (21.16)). Note that this assumes that the crust forms at the vent and survives down-flow to wherever the calculation takes place.

21.3.2. Viscosity Model

Fluid viscosity will vary from case to case depending on composition, water content, and temperature [e.g., Bottinga and Weil, 1972; Shaw, 1972]. The original FLOWGO model of Harris and Rowland [2001] used the Arrhenian model of equation (21.6) to allow the viscosity for the fluid phase of the lava mixture to be estimated as a function of temperature. This requires a value for the constant A that will vary depending on composition. For Hawaiian tholeiitic samples Shaw [1969] used a value of 0.02 K^{-1} for A , whereas Dragoni [1989] used a value of 0.04 K^{-1} for Etna. Solution of equation (21.6) also requires

Table 21.5 Average compositions used for FLOWGO models applied here with density calculated using Bottinga and Weill [1970].

Oxide	Generic ^a	Etna 91–93 ^b	ML 1984 ^c	ML 1859 ^d	Kīlauea ^e	Units
SiO ₂	51.63	47.93	52.32	51.6	51.43	wt%
Al ₂ O ₃	13.12	17.87	13.82	13.37	13.52	wt%
Fe ₂ O ₃	2.58	3.30	0.00	0.00	0.00	wt%
FeO	8.48	6.96	10.99	10.95	10.96	wt%
MgO	8.53	5.40	6.81	8.49	6.76	wt%
CaO	9.97	9.98	10.63	10.07	11	wt%
TiO ₂	2.63	1.74	2.11	2.06	2.44	wt%
Na ₂ O	2.28	3.82	2.36	2.26	2.37	wt%
K ₂ O	0.49	1.87	0.39	0.41	0.43	wt%
H ₂ O	0	0.1	0.1	0	0	wt%
Density	2774	2723	2724	2739	2744	kg/m
T_0	1200	1160	1200	1240	1200	°C
T_{erupt}	1140	1065	1140	1216	1154	°C
Slope	2.22	2.27	2.36	2.22	2.2	
Viscosity at T_0	20	42	44	14	19	Pa·s
Viscosity at T_{erupt}	39	129	86	18	30	Pa·s

Note: Also given are the liquidus (T_0) and eruption temperatures (T_{erupt}) plus the slope of the temperature – fluid viscosity relation that these compositions give (using the method of Shaw [1972]). Finally the fluid viscosities at T_0 and T_{erupt} calculated using the appropriate slope values in equation (21.18) are given.

^aTholeiitic composition for Mauna Loa given in Table 9.6 of Wilson [1989] using data taken, in turn, from the *Basaltic Volcanism Study Project* [1981].

^bEtna 91–93: Mean whole rock composition for Etna's 1991–1993 lava given in Table 3 of Tonarini *et al.* [1995]

^cML 1984: Mean whole-rock composition for Mauna Loa's 1984 lava given in Table 4 of Rhodes [1988].

^dML 1859: Glass composition for Mauna Loa's 1859 lava (mean from near-vent spatter samples) given in Appendix 2 of Riker *et al.* [2009].

^eKīlauea: Mean glass composition for upper elevation tube samples obtained for Kīlauea's episode 53 (1994–1997) eruption and given in Appendix 1A of Thornber [2001].

a value of the fluid viscosity at its liquidus temperature (η_0). Viscosity at liquidus can be calculated using a range of methods, as reviewed for Hawaiian and Etna lavas by *Harris and Allen* [2008]. One method is that of *Shaw* [1972], whereby fluid viscosity can be calculated as a function of composition and temperature following

$$\ln(\eta_f) = s(10^4/T) - sc_T + c_\eta, \quad (21.18)$$

in which s is the characteristic slope for the viscosity-temperature relationship of a given multicomponent mixture and c_T are c_η are temperature and viscosity-dependent constants with values of 1.5 and -6.4 , respectively. This gives η_0 of 14–44 Pa·s for the Hawaiian samples considered here and 42 Pa·s for the Etna samples (Table 21.5). The resulting $\eta_f(T)$ relationships defined by all three approaches considered here are plotted, for the Etna and Hawai'i cases of Table 21.5, in Figure 21.2.

However, the relationship of *Shaw* [1972] assumes an Arrhenian temperature dependence for viscosity, which may not be valid. As a result, in the updated version of FLOWGO presented here, we have adopted the Vogel-Tammann-Fulcher (VTF) equation as an empirical means of providing a best fit to available temperature and viscosity data for a given melt. This relationship is given by *Mano and Pereira* [2004] as

$$\log \eta(T) = D + \frac{E}{T(K) - F}, \quad (21.19)$$

D , E and F being adjustable (best-fit) parameters that depend on melt composition [e.g., *Hess and Dingwell*, 1996; *Whittington et al.*, 2001; *Zhang et al.*, 2003; *Giordano et al.*, 2006]. *Giordano and Dingwell* [2003] provide one such relationship for Etna lavas whereby

$$\log_{10}(\eta_f) = -4.643 + \frac{5812.44 - 427.04\text{H}_2\text{O}}{T_{\text{int}}(K) - 499.31 + 28.74\ln(\text{H}_2\text{O})}, \quad (21.20)$$

in which H_2O is the water content in wt% and $T(K)$ is lava temperature in Kelvin. As shown in Figure 21.2a, this provides a somewhat different temperature-dependent viscosity relationship for Etna lavas than that provided by *Dragoni* [1989] or *Shaw* [1972]. The cooling relation can now be used to up-date the lava temperature, estimate the crystal content based on the Table 21.6 look-up table, and calculate the fluid-crystal mixture viscosity by inserting any of the preceding equations as η_f into equation (21.5). These differing models can be folded into FLOWGO as described next.

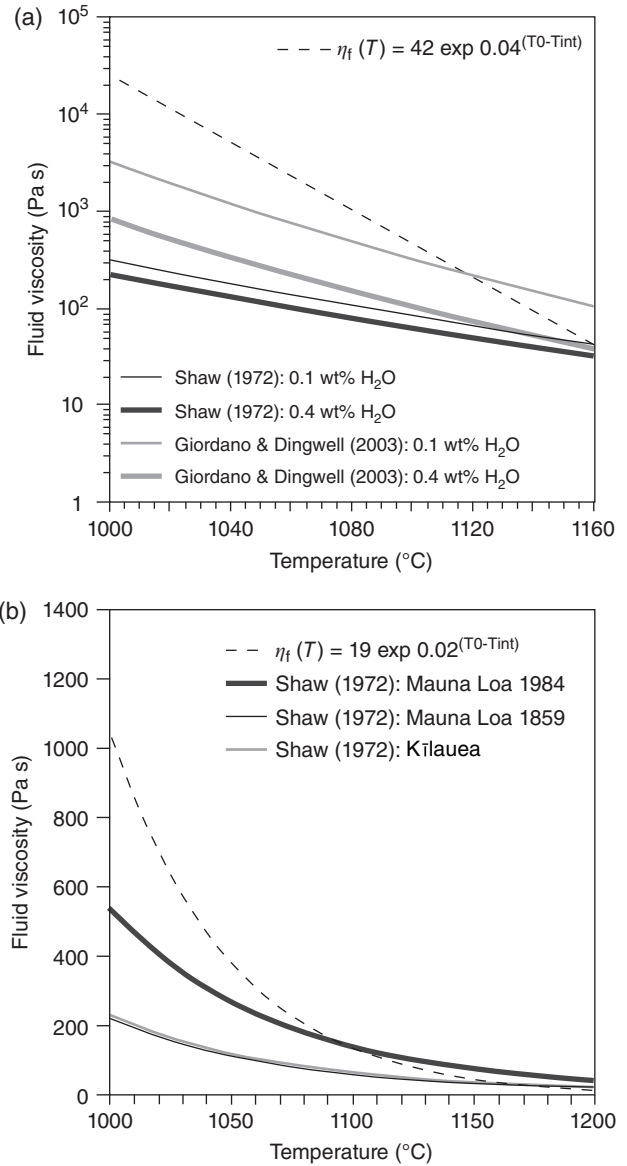


Figure 21.2 Temperature-dependent fluid viscosity relations used for (a) Etna and (b) Mauna Loa and Kīlauea.

21.3.3. Best-Fit Scenarios

The intent of FLOWGO was that the framework of input equations could be adjusted to test the applicability of different thermo-rheological models to different flow emplacement scenarios. For a given set of models, it would also allow thermo-rheological input parameters to be set and tested on a case by case basis (e.g., Tables 21.1 and 21.2). Field data for down-flow variations in channel width, velocity, internal temperature, and/or viscosity allow models and parameters to be adjusted to provide best-fit scenarios that likely describe the thermo-rheological emplacement conditions and their variation down-channel. We illustrate this using an example from Etna.

Table 21.6 Generic crystallization file used by FLOWGO.

Melt Temperature (°C)	Liquid Mass (g)	New Solids (g)	Solid Mass (g)	Total Mass (g)	Microlites Grown ($\delta\phi$)	Crystallization Rate ($\delta\phi/\delta T$)
1140	54.87		44.2	99.07		
1120	44.47	10.41	54.61	99.08	0.1051	5.25×10^{-3}
1100	32.55	11.95	66.56	99.11	0.1206	6.03×10^{-3}
1080	24.75	7.83	74.39	99.14	0.0790	3.95×10^{-3}
1060	20.85	3.92	78.31	99.16	0.0395	1.98×10^{-3}
1040	18.4	2.46	80.77	99.17	0.0248	1.24×10^{-3}
1020	16.63	1.77	82.54	99.17	0.0178	8.92×10^{-4}
1000	15.27	1.37	83.91	99.18	0.0138	6.91×10^{-4}
980	14.21	1.07	84.98	99.19	0.0108	5.39×10^{-4}
960	13.37	0.85	85.83	99.2	0.0086	4.28×10^{-4}
940	12.69	0.69	86.52	99.21	0.0070	3.48×10^{-4}
920	12.13	0.57	87.09	99.22	0.0057	2.87×10^{-4}
900	11.56	0.48	87.57	99.13	0.0048	2.42×10^{-4}
Total		43.37			0.4375	1.82×10^{-3}

Note: File is based on liquid and new solid masses calculated using the generic composition of Table 21.5 in MELTS and running the model in 10°C cooling steps between 1140 and 900°C. The mass fraction of microlites grown over each cooling step is obtained by dividing the new solids grown over that step by the total mass. Crystallization rate is then obtained by dividing the amount of microlites grown over each step (new solids) by the step range (10°C). Over the total cooling range of 240°C, a total mass of 43.37 g of new solids (microlites) are grown to give a volume fraction of crystallization of 0.4375 between 1140 and 900°C for this composition.

The starting conditions for a 1 m deep and 6 m wide channel active on Etna during September 2004 are given in Table 21.2. Excellent constraints on the dimensions of this channel are available, where cross-channel profiles were taken every 10 m down-channel from Lidar data by *Mazzarini et al.* [2007]. *Harris et al.* [2007] used the starting conditions of Table 21.2 to fit model output effusion rate, velocity, and width variation to these Lidar data. A best fit was achieved using a poorly insulated thermal surface over the first 350 m, with a crust temperature varying as a function of time and crust fraction as a function of velocity, following

$$T_{\text{crust}}(t) = -140 \log(t) + 303 \quad (21.21a)$$

and

$$f(V) = 1 \exp(-0.00756 v_{\text{mean}}). \quad (21.21b)$$

Beyond 350 m, a well-insulated model was applied in which crust coverage was total (i.e., $f=1$) and crust temperature was constant at 150°C. The resulting fit between model output and Lidar-derived channel width is given in Figure 21.3a.

To obtain this fit, at-vent crystal contents of 25%–30% were required (Figure 21.3a), and these values are lower than the typical phenocryst contents for Etna lavas of $34\% \pm 7\%$ [e.g., *Tanguy*, 1973; *Armienti et al.*, 1984; 1994]. Using the upper bounds of the typical range in our model for the 2004 flow causes the fit to break down (Figure 21.3b).

The original best-fit model [*Harris et al.*, 2007] used the viscosity model of equation (21.6), i.e., the relation of *Dragoni* [1989]. As seen in Figure 21.2a, this model may overestimate the fluid viscosity–temperature relation. If instead we use the empirical model derived for Etna lavas by *Giordano and Dingwell* [2003], i.e., the viscosity model of equation (21.20), a fit that can be applied over the full range of expected at-vent crystallinity conditions is obtained (Figure 21.3c). We can also cross-check at-vent model conditions, as given in Table 21.2, with available field measurements. Field measurements revealed maximum flow velocities of 0.7 m/s and effusion rates of 2–4 m³/s at a measurement point ~5 m from the vent (www.ct.ingv.it/Etna2004/Default.htm). The Lidar-derived flow volume of $1.1 \times 10^6 \pm 0.4 \text{ m}^3$ and an emplacement duration of ~6 days [*Mazzarini et al.*, 2007] also indicated a time-averaged discharge rate of $2.2 \pm 0.8 \text{ m}^3/\text{s}$. These flow velocities and effusion rates are consistent with our model output values when run with a starting crystal content of 34%–41%, as given in Table 21.2.

Thus, a fit can be obtained if we use a variable thermal surface with appropriate viscosity and crystallinity inputs, with the resulting model-based flow run-outs of 1.6–2.9 km being in line with the mapped channel length of 1.6 km and total (channel-fed) flow unit length of 1.625 km [*Mazzarini et al.*, 2007]. The maximum bound for our model-based estimate may suggest that the flow had not reached its full, cooling-limited potential at the time of Lidar data acquisition. Indeed, the empirical relation

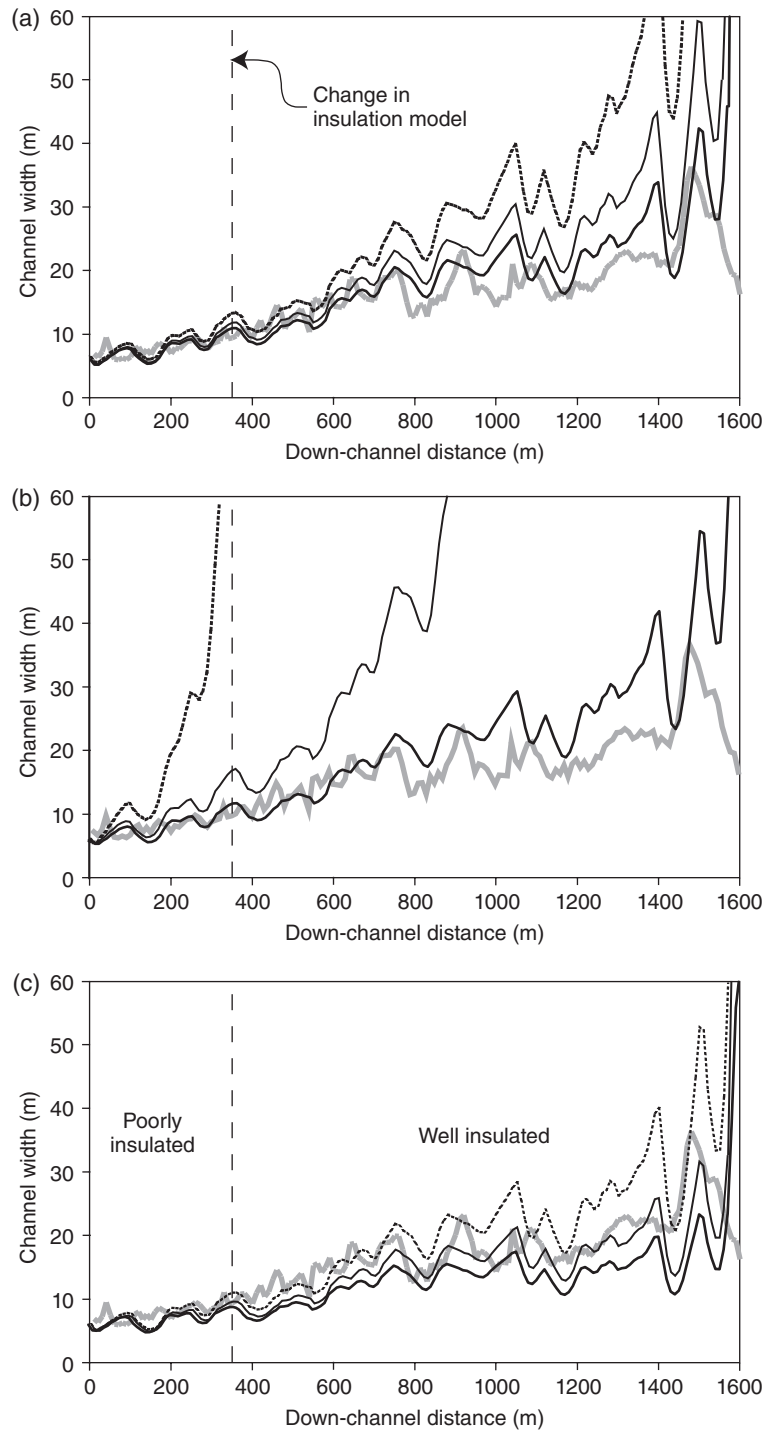


Figure 21.3 FLOWGO-estimated channel widths for Etna's September 2004 channel (black lines) and widths measured from the *Lidar* data of Mazzarini *et al.* [2007] (gray line). (a) Original-best fit of Harris *et al.* (2007) using the starting conditions of Table 21.2, the viscosity model of equation (21.6), and starting crystal (phenocryst) contents of 30% (dashed black line), 27.5% (solid black line, thin), and 25% (solid black line, thick). (b) Fit using the starting conditions of Table 21.2, the viscosity model of equation (21.6), and starting crystal (phenocryst) contents of 41% (dashed black line), 34% (solid black line, thin), and 27% (solid black line, thick). (c) Fit using the starting conditions of Table 21.2, the viscosity model of equation (21.20), and starting crystal (phenocryst) contents of 37% (dashed black line), 34% (solid black line, thin) and 27% (solid black line, thick).

between effusion rate and flow length (L) for Etna lavas given by *Calvari and Pinkerton* [1998], i.e., $L = 10^{3.11} E_r^{0.47}$ ($R^2 = 0.86$) indicates that this flow had the potential to extend 1.8 km at $2 \text{ m}^3/\text{s}$ and 2.5 km at $4 \text{ m}^3/\text{s}$, supporting our run-out estimates and prompting a similar conclusion.

21.4. THERMO-RHEOLOGICAL SIMULATIONS OF HAWAIIAN LAVAS

FLOWGO provides a framework within which to generate thermorheological histories for channel-contained lava control volumes. We demonstrate the best fits that can be obtained from FLOWGO plus some caveats in applying the model using three test cases from Hawai'i for which excellent control data exist, these being channel-fed flows active on Mauna Loa during 1984 and 1859 as well as on Kīlauea in 1974.

21.4.1. Mauna Loa: 1984

Initial tests by *Harris and Rowland* [2001] focused on fitting model output values to field measurements made during Mauna Loa's 1984 eruption. This eruption began during the afternoon of 25 March 1984 and continued until 14 April 1984, building a channel-fed lava flow field whose most distant unit extended 26.5 km from the vent [*Lipman and Banks*, 1987]. The two main channel-fed flow units active during the eruption (flows 1 and 1A) reached 90% of their maximum distance during their first 4 to 5 days of activity [*Rowland et al.*, 2005]. Flow 1 was active between 25 and 29 March, reaching its maximum length (~25 km) on 29 March, at which point a levee failure ~13 km behind the flow front robbed flow 1 of supply and began supply to flow 1A [*Lockwood et al.*, 1985]. Flow 1A began to extend rapidly parallel to flow 1 but did not overtake flow 1 until 4 April, reaching its maximum extent the following day, when it too was robbed of supply by a new levee collapse higher in the system [*Lockwood et al.*, 1985]. Effusion rates peaked at ~800 m^3/s during the first day of the eruption, before falling to lower levels over the next 12 days [*Lipman and Banks*, 1987]. *Rowland et al.* [2005] pointed out that early in the eruption, when effusion rate was high, there was no well-established channel and lava lost considerable energy flowing as unconfined sheets of dispersed flow over rough ground. With time, a stable channel developed [*Lipman and Banks*, 1987] to allow more efficient delivery of lava to the flow front. However, by this time the effusion rate had decreased, meaning that the highest effusion rate never coincided with the greatest length of efficient, stable channel.

Because FLOWGO models the thermo-rheological evolution of a control volume moving down an established channel, and not advance of a flow front, FLOWGO is thus initialized with the effusion rates that fed the

channel, and then outputs velocities and travel times for lava flowing in the same stable channel. In the case of Mauna Loa's 1984 flow this means that data for the established, stable channel feeding flows 1 and 1A on or after day 4 (29 March) are appropriate as input. Data by *Lipman and Banks* [1987] give effusion rates measured for these flows in the range 100–440 m^3/s between 29 March and 5 April (when flow 1 had reached its maximum extent and flow 1A was active), with peaks of ~1140 and 945 m^3/s being recorded at the main vent outlet on 2 April and 4 April, respectively. An effusion rate of 900 m^3/s was also recorded on 6 April. These peak values corresponded to maximum flow velocities measured in the at-vent channel of 17.65 m/s on 2 April and ~15 m/s on 4 and 6 April. At this point, the channel at the main vent outlet had a depth of 3 m and a width of between 20 and 21.5 m [Table 57.3 of *Lipman and Banks*, 1987]. At the same time, *Moore* [1987] calculated a viscosity of 140 Pa·s for lava at the vent on 2 April, increasing down-channel to $1.0\text{--}1.3 \times 10^3$ Pa·s at 3 km, $3.0\text{--}9.5 \times 10^3$ Pa·s at 9 km, $0.9\text{--}1.6 \times 10^5$ Pa·s at 15 km, and 5.6×10^6 Pa·s at 26 km (at the toe of flow 1A). At the same time, near-vent yield strength was calculated as being between 66 and 220 Pa [*Moore*, 1987].

21.4.1.1. Original and Updated Model Fits

The original model runs of *Harris and Rowland* [2001] used two end-member models, hot and cool. These models, as given in Table 21.7, were set to cover the full range in uncertainty in the various thermo-rheological conditions used to initialize the model. The two models yielded a maximum distance that lava flowing in the channel could extend of 23.7 km (hot model) and 30 km (cool model). At-vent viscosity, yield strength, velocity, and effusion rate are also given in Table 21.7 and show reasonable agreement with the field data for near-vent conditions given above. Comparisons between down-channel variations in model-derived and field-measured velocity, width, and temperature also showed reasonable fits (Figures 21.4a–c). However, some of the thermo-rheological relations used for the original best-fit model are not necessarily appropriate, with the viscosity relation being more appropriate for Etna lava and the surface cooling at the same rate as the core. In addition, while modeled at-vent viscosities and velocities were a little high, yield strengths were a little low (Table 21.7).

We here experiment with an updated version of the model which allows us to maintain these fits while using more appropriate input parameters and thermo-rheological models, as given in Table 21.8. This uses a viscosity relation set for the composition of Mauna Loa's 1984 lava, as given in Table 21.5, and a surface crust that cools with time and distance from the vent. The model output now spans a wider range of distances; 17.5 km (hot model) and 28 km (cool model). However, fits between modeled at-vent viscosity, yield strength,

Table 21.7 Cool and hot models applied to provide best fits to the 1984 Mauna Loa channel conditions by *Harris and Rowland* [2001].

Parameter (term, units)	Model Value		Source
	Cool	Hot	
Channel width (w , m)	5.5	5.5	Mean channel width from all values given in Table 57.3 of <i>Lipman and Banks</i> [1987] for channel stations below the 1900 m elevation level
Channel depth (d , m)	5.5	5.5	Square channel ($w=d$)
Air temperature (T_{air} , °C)	10	30	
Eruption temperature (T_{erupt} , °C)	1137	1143	Mean ($\pm 1\sigma$) eruption temperature given by <i>Lipman and Banks</i> [1987]
Solidus temperature (T_{solid} , °C)	970	990	
Phenocryst content (ϕ_{phen})	0.15	0.00	Range given by <i>Lipman and Banks</i> [1987] for the period 25–28 March 1984
Posterupture crystallization (ϕ_{post})	0.45	0.45	Posterupture crystallization calculated using MELTS
Crystallization rate ($\delta\phi/\delta T$)	—	—	Value for linear crystallization model [<i>Harris and Rowland</i> , 2001]: $\delta\phi/\delta T = \phi_{\text{post}} / (T_{\text{erupt}} - T_{\text{solid}})$
Crust temperature (T_{crust} , °C)	425	675	Approximate crust temperature range obtained at the margins of an active channel on Kīlauea by <i>Flynn and Mouginis-Mark</i> [1994]
Crack temperature (T_{hot} , °C)	A	B	Model A: $T_{\text{hot}} = T_{\text{core}} - 140$; model B: $T_{\text{hot}} = T_{\text{core}} - 0$
Basal contact temperature (T_{base} , °C)	500	900	Based on a value of $700 \pm 200^\circ\text{C}$ from <i>Keszthelyi</i> [1995] and <i>Wooster et al.</i> [1997]
Basal crust thickness (H_b , %)	19	1	
Vesicularity (%)	1	15	Vesicularity range calculated from all bulk density data of <i>Lipman and Banks</i> [1987]
Crust cooling model	Fixed at vent: cools down flow as a function of core cooling rate $f(V) = x \exp(yV_{\text{mean}})$, $x = 0.9023$, $y = -0.1601$ [<i>Harris and Rowland</i> , 2001] Arrhenian model (Equation 21.6) with $\eta_0 = 1000 \text{ Pa}\cdot\text{s}$, $T_0 = T_{\text{erupt}}$ $A = 0.04 \text{ K}^{-1}$		
Crust coverage model			
Rheological model			
Output			
At-vent viscosity (η , Pa s)	1900	1000	Viscosity for mixture of fluid and crystals
At-vent yield strength (τ_0 , Pa)	29	0	Yield strength for mixture of fluid and crystals
At-vent velocity (V_{mean} , m/s)	13.3	21.7	
Effusion rate (E_r , m ³ /s)	402	656	
Distance (km)	28.77	23.69	

velocity, and effusion rate and field data are improved over the original runs (Table 21.8). These new fits between down-channel variations in model-derived and field-measured velocity, width, and temperature are given in Figures 21.4d–f.

21.4.1.2. The Viscosity Problem

For both the original and updated models, we note a problem when trying to fit down-flow variation in viscosity to the 2 April 1984 field data of *Moore* [1987]. The problem being that we underestimate the expected viscosity at all down-flow points after the vent (Figure 21.5a). The difficulty in matching the viscosities obtained by *Moore* [1987] when using a fluid viscosity calculated using the work of *Shaw* [1972] and the flow crystal content in a mixture viscosity calculation based on the Einstein-Roscoe relation (as given in equation (21.5)) was

noted by *Crisp et al.* [1994]. *Crisp et al.* [1994] suggested that this difficulty was likely due to the failure to take into account the influence of bubbles on the mixture viscosity. *Harris and Allen* [2008] thus were able to match all of *Moore's* [1987] viscosity regimes using appropriate crystallinity and vesicularity values in the three-phase viscosity treatment of *Phan-Thien and Pham* [1997].

Following *Harris and Allen* [2008], we obtain a fit with at-vent viscosity if we use the three-phase model of viscosity as given in equation (21.10) and the starting conditions of the FLOWGO hot model set up for Mauna Loa's 1984 channel (Figure 21.5b). To obtain this at-vent fit, we have to apply a case whereby the vesicles have no effect on the mixture viscosity and use a phenocryst content of 15%, this being the minimum phenocryst content during 2–6 April [*Lipman and Banks*, 1987]. However, hot model viscosity predictions for all

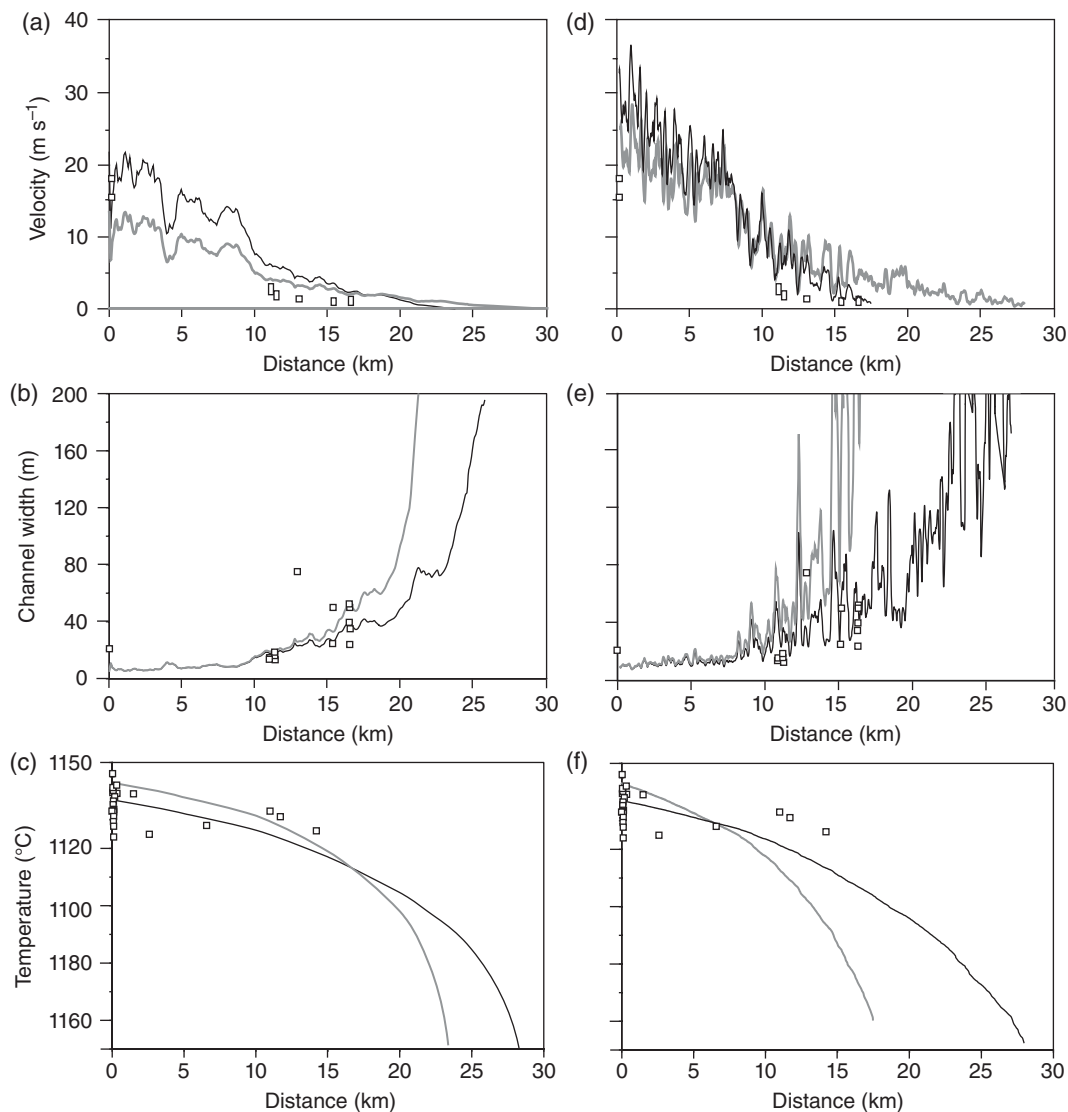


Figure 21.4 Original (a–c) and updated (d–f) FLOWGO runs for Mauna Loa’s 1984 channel. Results for velocity, channel width, and interior temperature are given. For both cases results of two end member models are given as calculated using a “hot” model (gray line) and “cold” model (black line). Down-channel field measurements for velocity, channel width, and lava interior temperatures are from *Lipman and Banks* [1987] and are given using open squares. The original model is run using the initialization parameters given in Table 21.7, with an Arrhenian viscosity relation set for Etna’s lava, as used by *Harris and Rowland* [2001] for initial model tests on this channel. The updated model is run using the initialization parameters given in Table 21.8, with an Arrhenian viscosity relation set using *Shaw* [1972] and a chemistry appropriate for this lava, as given in Table 21.5.

other points down-channel remain far too low and the flow run out distance is too far. To obtain a fit with viscosity between 3 and 9 km requires application of the cold model and the three-phase viscosity treatment applied using a bubble content of 43% and phenocryst content of 29% (Figure 21.5b). Both are values that are within the bounds of those measured at this channel, with 30% being the maximum phenocryst content given by *Lipman and Banks* [1987] and 43% being the maximum vesicularity calculated from the density

measurements made on channel samples by *Lipman and Banks* [1987]. However, we can only achieve the fit if we assume a Newtonian flow regime. That is, we have to assume that the lava has no yield strength and drop the second term of equations (21.1b,c), thus reverting to equation (21.1a). After 10 km we can only obtain a fit if we also alter the thermal surface model to one of well-insulated flow conditions whereby the flow surface has a total coverage of crust at 125°C after this point (Figure 21.5c).

Table 21.8 Updated FLOWGO model run with Mauna Loa 1984 vent channel dimension data and parameter ranges for 2–6 April when flow 1A was active.

Parameter (term, units)	Model Value		Source
	Cool	Hot	
Channel width (w , m)	21	21	Typical channel width and depth at 2850m vent outlet given in Table 57.3 of <i>Lipman and Banks</i> [1987] for the period 2–6 April 1984 (days 8–12)
Channel depth (d , m)	3	3	
Air temperature (T_{air} , °C)	10	30	Mean ($\pm 1\sigma$) eruption temperature given by <i>Lipman and Banks</i> [1987]
Eruption temperature (T_{erupt} , °C)	1137	1143	
Solidus temperature (T_{solid} , °C)	970	990	Range given by <i>Lipman and Banks</i> [1987] for the period 2–6 April 1984
Phenocryst content (ϕ_{phen})	0.14	0.25	
Posteruption crystallization (ϕ_{post})	0.45	0.45	Posteruption crystallization calculated using MELTS
Crystallization rate ($\delta\phi/\delta T$)	0.0027	0.0029	Value for linear crystallization model [<i>Harris and Rowland</i> , 2001]: $\delta\phi/\delta T = \phi_{\text{post}} / (T_{\text{erupt}} - T_{\text{solid}})$
Crust temperature (T_{crust} , °C)	Variable	Variable	Calculated as a function of time equation (21.13)
Crack temperature (T_{hot} , °C)	A	B	Model A: $T_{\text{hot}} = T_{\text{core}} - 140$; Model B: $T_{\text{hot}} = T_{\text{core}} - 0$
Basal contact temperature (T_{base} , °C)	500	900	Based on a value of $700 \pm 200^\circ\text{C}$ from <i>Keszthelyi</i> [1995] and <i>Wooster et al.</i> [1997]
Basal crust thickness (H_b , %)	19	1	Vesicularity range calculated from bulk density data for channel samples given in Table 57.1 of <i>Lipman and Banks</i> [1987]
Vesicularity (%)	14	43	
Crust cooling model	Crust cools as a function of distance and time from vent Equations (21.16) and 21.17		
Crust coverage model	$f(V) = x \exp(yV_{\text{mean}})$, $x = 0.9$, $y = -0.16$ [<i>Harris and Rowland</i> , 2001]		
Rheological model	Model of <i>Shaw</i> [1972], i.e. equation (21.18) with the slope calculated using the ML1984 chemistry of Table 21.5		
Output			
At-vent mixture viscosity (η , Pa·s)	292	151	Viscosity for mixture of fluid and crystals
At-vent yield strength (τ_0 , Pa)	126	24	Yield strength for mixture of fluid and crystals
At-vent velocity (V_{mean} , m/s)	10.3	13.8	
Effusion rate (E_r , m ³ /s)	647	869	
Distance (km)	27.95	17.46	

This suggests a complex thermo-rheological regime, which requires application of a hybrid model that evolves down-channel if we are to obtain the best possible fit with all available field data. We suggest that at least three flow thermo-rheological regimes existed on 2 April: (1) a poorly insulated regime over the first 3 km across which vesicularities were high but vesicles were sheared so that they had little effect on the mixture viscosity; (2) a poorly insulated regime between 3 and 10 km across which vesicularities were high but vesicles were less sheared so that they served to increase the mixture viscosity as the crystal content also increased; and (3) an insulated flow regime over the remaining channel length with both vesicles and crystals contributing to the viscosity gain. The need for such a down-channel-evolving

thermo-rheological regime was suggested by *Moore* [1987], who stated that “it is entirely possible that the Mauna Loa lava obeyed different flow laws at different places and times the lava may have been a Newtonian fluid at the vents, a Bingham fluid at station 8, and a pseudoplastic fluid or some other kind of fluid in other reaches” [*Moore*, 1987, pp. 1555–1586]. In addition, to account for a change in bulk volume flux between the vent and 15 km, the lava bulk density had to have increased by a factor near 12 [*Moore*, 1987], pointing to a down-channel decrease in vesicularity alongside a cooling-induced increase in crystallinity, with maximum downstream crystallinity (of 39%, comprising 25% microlites and 14% microphenocrysts) being found in a quenched sample 14 km from the vent by *Crisp et al.*

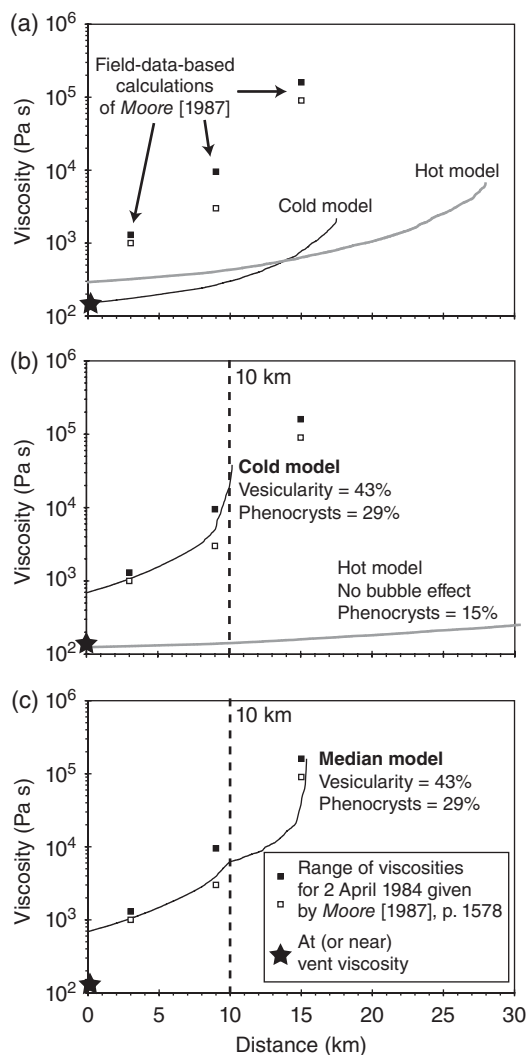


Figure 21.5 FLOWGO viscosity best-fit simulations for Mauna Loa's 1984 channel. (a) Shaw [1972] in the Einstein-Roscoe equation with a 15% phenocryst content and the time-dependent crust cooling (and hence heat loss) model of equation (21.16). (b) Shaw [1972] in the three-phase viscosity treatment of Phan-Thien and Pham [1997] with the time-dependent crust cooling (and hence heat loss) model of equation (21.16). (c) Shaw [1972] in the three-phase viscosity treatment of Phan-Thien and Pham [1997] with the time-dependent crust cooling (and hence heat loss) model until 10 km and an insulated model of complete crust coverage at 125°C thereafter. Models in (b) and (c) are Newtonian.

[1994]. This compares with a total crystallinity of 28%–31% obtained using our hot model at a distance of 14–15 km (14%–17% microlites, 14% microphenocrysts), with 25% microlites being grown by 17 km. Hence, the fluid-crystal-bubble mixture viscosity would have evolved as a function of not just vesicularity but also crystallinity.

Finally, at ~15 km Moore [1987] described a flow surface that was “a hummocky mass of slowly moving debris, rubble and blocks” compared with a more poorly crusted channel with incandescent zones nearer the vent. This indicates a change in the thermal surface character from poorly to well insulated between the proximal and medial-distal reaches. Clearly, the thermal and rheological conditions, as well as the associated flow regimes, changed significantly down-channel, necessitating application of a highly flexible thermo-rheological model, as we have had to do here.

21.4.2. Mauna Loa: 1859

Mauna Loa's 1859 eruption produced a 51 km long channel-fed flow field fed at effusion rates of ~391 m³/s during the period of channel lengthening [Riker *et al.*, 2009]. This case can be used to demonstrate the best-fit approach in applying FLOWGO.

Initial fits between expected down-channel variation in lava temperature and crystallinity and those obtained using FLOWGO by Riker *et al.* [2009] were poor (Figure 21.6). Given that these fits were achieved using an unrealistic crystallization model as well as an inappropriate thermal and rheological model, the failure is not too surprising. As discussed by Riker *et al.* [2009], the default MELTS-based crystallization model used by FLOWGO is only appropriate up to temperatures of 1140°C (see Table 21.6), where eruption temperatures were as high as 1216°C [Riker *et al.*, 2009]. The MELTS-based crystallization model of FLOWGO also considers a tholeiitic composition for Mauna Loa as given in Table 9.6 of Wilson [1989] using data taken, in turn, from the *Basaltic Volcanism Study Project* [1981]. In addition, while the viscosity model used in the model runs of Riker *et al.* [2009] was appropriate to an Etna lava, the thermal (and crystallization) regime appeared to change down-channel. Interior cooling, for example, appeared to show a rather steep declining trend until 10 km and a trend of ~0.5°C/km thereafter (Figure 21.6). We therefore prefer to produce a best fit to this flow using appropriate input data and a hybrid model.

It is apparent from the data of Riker *et al.* [2009] that there were two cooling and crystallization regimes: (1) rapid cooling and crystallization between the vent and 10 km and (2) slower cooling and crystallization thereafter. Over the first 10 km, temperatures dropped from 1216 to 1160°C at a rate of 5.6°C/km, thereafter showing a steady, slower decline to 1146°C by 36 km at a rate of 0.5°C/km [Riker *et al.*, 2009]. Thus, we set up a hybrid model that applies one set of (poorly insulated) thermal and crystallization conditions above 10 km and a second (well-insulated) set of conditions below 10 km. Also, we need to adapt the viscosity model to be appropriate for the temperatures and composition relevant to this flow. To do this, we use the method of Shaw [1972], as given

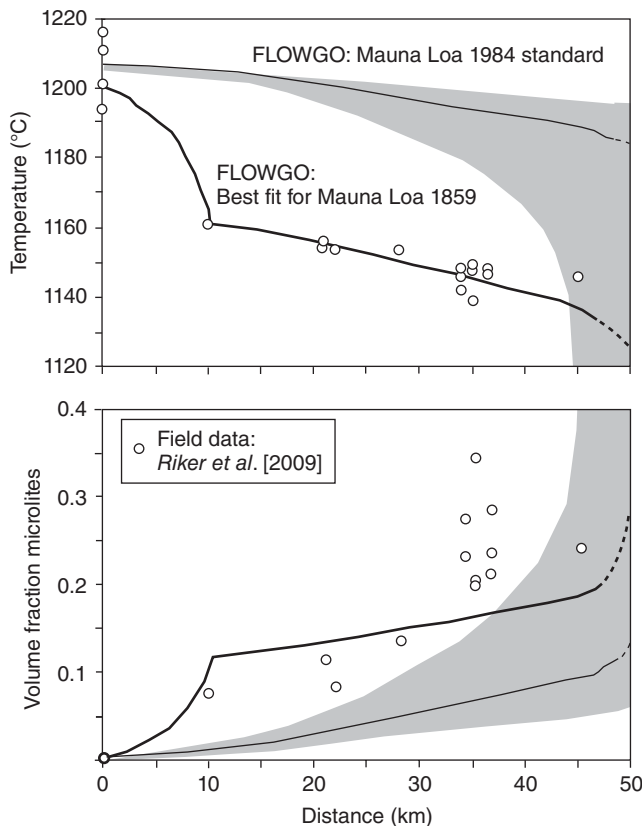


Figure 21.6 Comparison of FLOWGO model results and field data from the channel-fed phase of Mauna Loa's 1859 eruption as given by Riker *et al.* [2009] in their Figure 14. Input parameters are the standards set for Mauna Loa's 1984 eruption by Harris and Rowland [2001], and shaded regions show range of model results obtained by Riker *et al.* [2009] when input viscosity, vesicularity, and starting channel dimensions were varied within reasonable limits (10–1000 Pa·s, 8–40%, and 4.0–4.5 m, respectively). Comparison is given with a new hybrid FLOWGO run set up to provide a best fit to the field data of Riker *et al.* [2009], where (a) is a fit with down-flow interior temperature versus distance traveled and (b) fits the model to the volume fraction microlites grown versus distance.

here in equation (21.18), with a slope calculated for the composition of Mauna Loa's 1859 lavas as given in Table 21.5. Our revised FLOWGO input parameters for Mauna Loa's 1859 channel are given in Table 21.9. If we apply this hybrid model, we achieve excellent fits with the expected down-channel variation in crystallinity and temperature (Figure 21.6) as well as viscosity (Figure 21.7), producing a run out of 45.6 km at an effusion rate of $399 \text{ m}^3/\text{s}$ and interior temperatures at 10 and 36 km of 1159 and 1145°C , respectively. In achieving this fit, as with our Etna 2006 and Mauna Loa 1984 fits, the most crucial adjustments were to input (i) an appropriate crystallization model, (ii) an appropriate viscosity model, and (iii) a thermal surface whose character varied

down-channel between a poorly insulated proximal reach and a well-insulated medial-distal reach.

21.5. FLOW PATH AND RUN-OUT PROJECTIONS OF HAWAIIAN LAVAS

The initial FLOWGO model used the simple line of steepest descent, or deterministic eight-neighbor (D8) model [Mark, 1984; O'Callaghan and Mark, 1984], to set a flow line. This approach is not dissimilar to standard watershed models used in GIS to determine the channels water will take to exit a drainage basin via the highest order stream. In FLOWGO, the D8 model is corrected to allow flow lines to escape pits, basins and data drop-out holes in the DEM as well as to extend across flat zones [Fairfield and Leymarie, 1991; Turcotte *et al.*, 2001; Jones, 2002] so that a line of steepest descent is projected from the selected lava source (vent) to the edge of the DEM. FLOWGO then uses this line to extract a slope profile and uses this to estimate each thermo-rheological parameter at each point along the line.

Later, the flow path model was upgraded through combination with the DOWN-FLOW model of Favalli *et al.* [2005]. The DOWN-FLOW model finds the line of steepest descent, adds random noise to the DEM (which is equal to the DEM vertical resolution), and then finds the new path. This new path will be slightly different from the first due to the slight alteration of the DEM by addition of noise. The process is repeated until a field of flow paths is generated. This, in effect, provides the range in uncertainty of the flow line projection given that we are working with a quantized version of the terrain, with limits set (and potential topographic error being induced) by both the pixel size and DEM vertical resolution. We then run FLOWGO down each potential line of steepest descent.

We next consider output from the combined FLOWGO-DOWN-FLOW model for three cases for which we have reasonable control on effusion rates, down-flow thermo-rheological parameters, and flow length channel-fed lava flow units: Mauna Loa's 1984 flow units plus the 1859 flow and as Kilauea's 1974 flow. We note that we are using DEMs in which these flow fields already exist as topographic highs. They will thus influence the flow line, which will not follow the same path as the original flow. Thus, our objective is not to re-create these flows but to assess the validity of the combined thermorheological and flow line projections. We are thus looking at fictional flows that have similar properties to the existing flows and are flowing over roughly similar terrain (albeit with the 1859, 1974, and 1984 flows in place). These new flow paths may differ from the historical paths but will be influenced by similar topography (e.g., regional slopes, valleys, hills, cones, preexisting local flow margins, levees, and fronts).

Table 21.9 FLOWGO input parameters for Mauna Loa's 1859 channel simulation.

Parameter (term, units)	Model Value		Source
	<10 km	>10 km	
Channel width (w , m)	4	—	Starting condition of <i>Riker et al.</i> [2009] uses width of 4.0–4.5 m
Channel depth (d , m)	2	—	Square channel ($w=d$)
Air temperature (T_{air} , °C)	20	—	
Eruption temperature (T_{erupt} , °C)	1205	—	Midpoint of range of temperatures obtained by <i>Riker et al.</i> [2009] from lower vent spatter samples (range 1194–1216°C)
Phenocryst content (ϕ_{phen})	0.02	0.02	Typical values from Appendix 3 of <i>Riker et al.</i> [2009]
Posteruption crystallization (ϕ_{post})	0.05	0.3	Approximate crystal volume fractions grown above and below 10 km [see Figure 6a of <i>Riker et al.</i> , 2009]
Temperature range (δT , °C)	60	20	Approximate temperature decline above and below 10 km [see Figure 6b of <i>Riker et al.</i> , 2009]
Crystallization rate ($\delta\phi/\delta T$)	0.00083	0.015	Value for linear crystallization model: $\delta\phi/\delta T = \phi_{post}/\delta T$
Crack temperature (T_{hot} , °C)	B	B	Model A: $T_{hot} = T_{core} - 140$; model B: $T_{hot} = T_{core} - 0$
Basal contact temperature (T_{base} , °C)	500	500	
Basal crust thickness (H_b , %)	19	19	
Vesicularity (%)	40	25	Typical vesicularity values given for 'a'a channel samples in Figure 9 of <i>Riker et al.</i> [2009]
Crust cooling model	PI	—	Crust cools as a function of distance and time from vent Equations (21.16) and (21.17)
	—	WI	Stable (constant) crust temperature at value calculated for the 10 km position (480°C)
Crust coverage model	PI	—	$f(V) = x \exp(yV_{mean})$, $x = 0.9023$, $y = -0.04778$: poorly crusted
	—	WI	$f(V) = x \exp(yV_{mean})$, $x = 0.9023$, $y = -0.03652$: more heavily crusted
Rheological model	Model of <i>Shaw</i> [1972], i.e. Equation (21.18) with the slope calculated using the ML1859 chemistry of Table 21.5		

Note: Models: PI=poorly Insulated, WI=well Insulated.

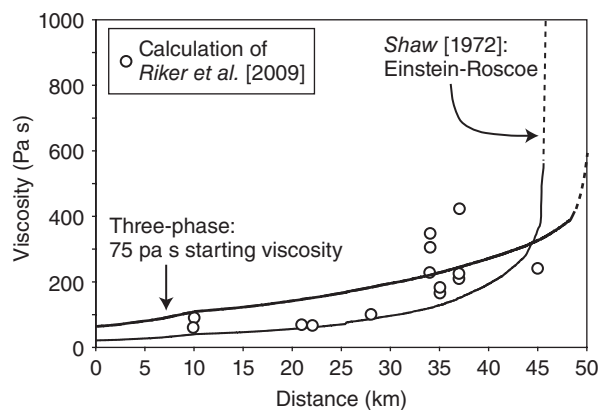


Figure 21.7 FLOWGO viscosity best-fit simulations for Mauna Loa's 1859 channel. Model is run using (i) a two-phase (melt and crystal) viscosity model and (ii) a three phase (melt, crystal, and bubble) viscosity model. Output is compared with the viscosities expected by *Riker et al.* [2009].

21.5.1. Mauna Loa: 1984

If we pick a vent location at the lower end of the Mauna Loa 1984 fissure system, we obtain a flow line projection that follows flow 1 for about a third of its total length (~8 km). At this point, the flow line falls off of flow 1 and takes a path parallel to the northern edge of the 1984 lava flow field, with the control volume advancing 26.7 km down that path to stop just short of the flow 1A toe (Figure 21.8a). To obtain this length, the model requires an effusion rate of 500 m³/s and gives at-vent velocity of 16.7 m/s.

The problem is, our DEM is from 2000 and therefore contains the 1984 flow field, which, locally, creates a topographic high. In such a case, on reaching the edge of the lava pile, the flow line projection will drop off of that pile and then follow the base of its marginal levee. Thus, we cannot re-create the path of the 1984 flow using this DEM because the flow itself is already there. However, we do project the likely path that a new flow erupted from a similar vent position and subject to the topographic control exerted by the presence of the 1984 flow field will now follow.

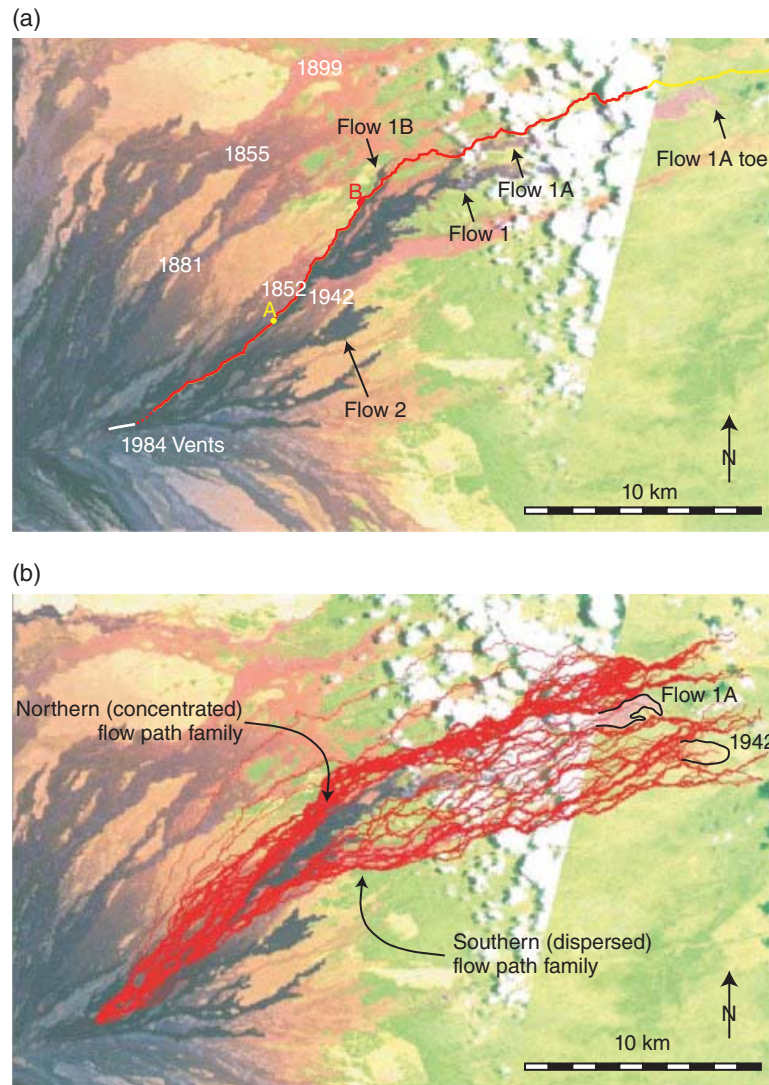


Figure 21.8 (a) FLOWGO single-path and (b) FLOWGO-DOWN-FLOW projections for a control volume advancing from the lower portion of Mauna Loa's 1984 eruptive fissure with the starting conditions of Table 21.1. (a) Yellow line projects the line of steepest descent between the designated vent position to the edge of the DEM. The red line gives the distance down the projection a FLOWGO control volume will advance. At point A, the projected path falls off of the local topographic high presented by the 1984 flow field and at B the projection encounters small basin, which is filled with the flow line leaving from the lowest elevation point around the basin rim. (b) Path and runout results for a 1000 iteration run at an effusion rate of 300 m³/s, with DEM noise of 2 m and a channel aspect ratio of 1. In both cases, base image is a 30 m spatial resolution Thematic Mapper color composite linked to the underlying DEM, and flow units are located following Figure 57.1b of *Lipman and Banks* [1987].

We next run the flow path model iteratively (1000 iterations, DEM noise 2m, square channel) from a vent location toward the lower end of the 1984 eruptive fissure and in the vicinity of the vent that fed the 1942 flow. At an effusion rate of 300 m³/s, a rate typical of that feeding Mauna Loa's 1984 channel [Rowland *et al.*, 2005], we find that the flow run-outs approximate the distances obtained by both the 1984 and 1942 flows, to give an average run-out of 27.4 km (Figure 21.8b). We note that the family of paths that extend in the direction of the 1984 flow field divide to flow down either side of that flow field, so that two families of flow

paths develop: to the north and south of the 1984 flow field, respectively (Figure 21.8b). This is a result of the 1984 flow field now being a local topographic high, around which a fluid will flow. To the south, the family of flow lines is somewhat more dispersed and encompasses the path of the 1942 flow. To the north, the flow line distribution is somewhat more concentrated, defining a dense zone of flow path concentration down the northern margin of the 1984 flow field. The presence of the 1984 flow field also creates a series of shadow zones, including a zone just downslope of the flow front (Figure 21.8b).

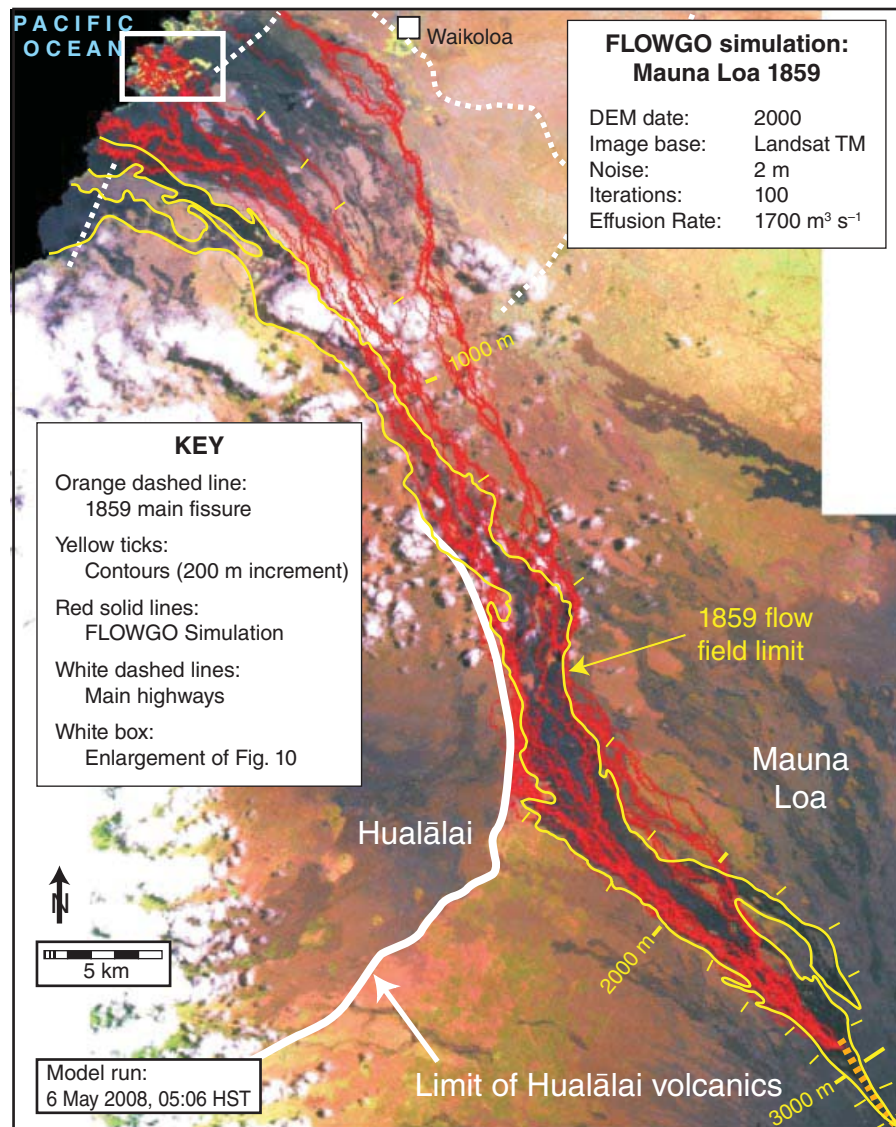


Figure 21.9 FLOWGO-DOWN-FLOW simulation of Mauna Loa's 1859 flow. Base image is a 30 m spatial resolution Thematic Mapper color composite linked to the underlying DEM and approximate flow field perimeter is located following Figure 3 of *Riker et al.* [2009]. White box locates the coastal section of the simulation as enlarged in Figure 21.10.

21.5.2. Mauna Loa: 1859

Running the DOW-FLOW path model iteratively (100 iterations, DEM noise 2 m, square channel) from a vent location within Mauna Loa's 1859 eruptive fissure, we obtain a family of flow paths that matches the area of the actual flow field quite well (Figure 21.9). One family of flow lines strays to the north of the actual flow. Again, this is a result of the flow field being present in the DEM and thus influencing the post-1859 path projections, deflecting them north once they have fallen off the flow itself.

Across the coastal zone (after a down-flow distance of $\sim 45 \text{ km}$ and within $\sim 5 \text{ km}$ of the coast), slopes decline to less than 1° (average 0.4°). An effusion rate of $1000 \text{ m}^3/\text{s}$ ensures that the control volume arrives at the back of the coastal zone, giving run-outs that stop just short of Queen Ka'ahumanu highway. An increase to $1700 \text{ m}^3/\text{s}$ is required if the control volume is to advance the final 2–3 km, over the flat coastal zone, and enter the ocean. Across the coastal zone the family of flow lines also begins to spread, as the actual flow field did, to cut a broad swath of the main highway serving Hawai'i's Kona and Kohala coasts and covering land now

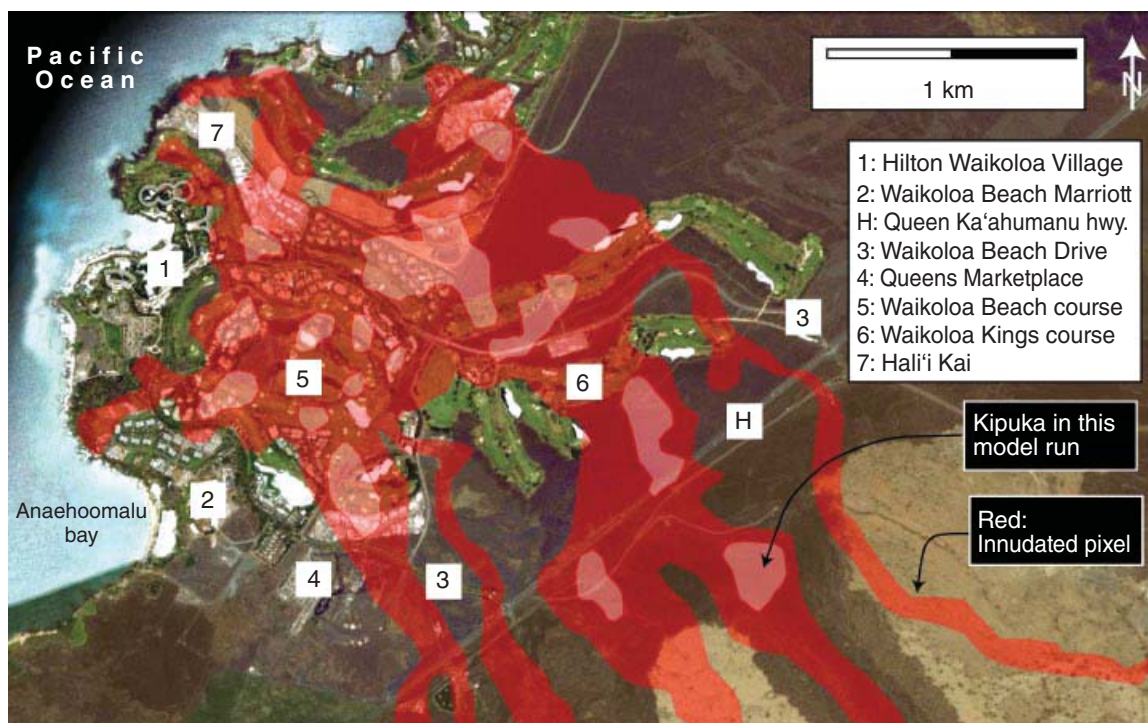


Figure 21.10 Enlargement of the coastal section of the FLOWGO-DOWN-FLOW simulation of Mauna Loa's 1859 flow given in Figure 21.9. Simulation is overlain on the Google Digital Globe [©2010] image of the Waikoloa resort.

occupied by Kona resorts and their associated golf courses (Figure 21.10).

The greens on the golf courses actually cause the flow lines to congregate or be deflected. While some lines follow the fairway edges (where they are raised), others are drawn down the line of the course, ponding within the greens or jumping from green to green. This is a result of the man-modified terrain that comprises topographic highs and lows in the surrounding lava that was locally cleared, heaped, and/or graded to construct the course. The two courses (Beach and Kings) were opened in 1981 and were thus not present during the emplacement of the 1859 flow. As a result, such modern man-made topography would not have had an influence on the 1859 flow field emplacement, the change in slope at the coast being the primary influence on the flow field form to cause distal spreading. However, the golf courses could influence flow paths should a similar effusive event occur today, with the courses possibly guiding the flows between and/or around the main resort structures, which are located just to the north and west (Hilton Waikoloa Village) as well as to south (Waikoloa Beach Marriott Resort & Spa) of the two courses. Certainly, all flow paths skirt north of the Waikoloa Beach Marriott Resort & Spa following the line of the Beach course,

which also keeps the same flow paths just south of the Hilton Waikoloa Village.

A clever but unintentional piece of resort design to guard against lava flow inundation in a hazardous location? Of course, there is plenty of infrastructure and real estate within the two courses themselves (especially the Beach course), but could well placed and well-designed golf courses and tourist infrastructure be used as subtle defense structures in zones prone to lava inundation?

21.5.3. Kīlauea: 1974

Kīlauea's December 1974 eruption began from a ~700 m long fissure that opened in the upper East Rift Zone. First fountains were sighted at 02:56 Hawaiian standard time (HST). These fed "extremely fluid" lava that built a flow field with a total volume of $5.9 \times 10^6 \text{ m}^3$ [Lockwood *et al.*, 1999]. The eruption ended around 08:50 HST the same day to give a mean output rate over the ~6 hour-long event of $270 \text{ m}^3/\text{s}$; peak effusion rates were probably higher. The 12.4 km long flow contained a 10 km long channelized segment, down which cooling rates were $1^\circ\text{C}/\text{km}$ across medial to distal portions [Soule *et al.*, 2004].

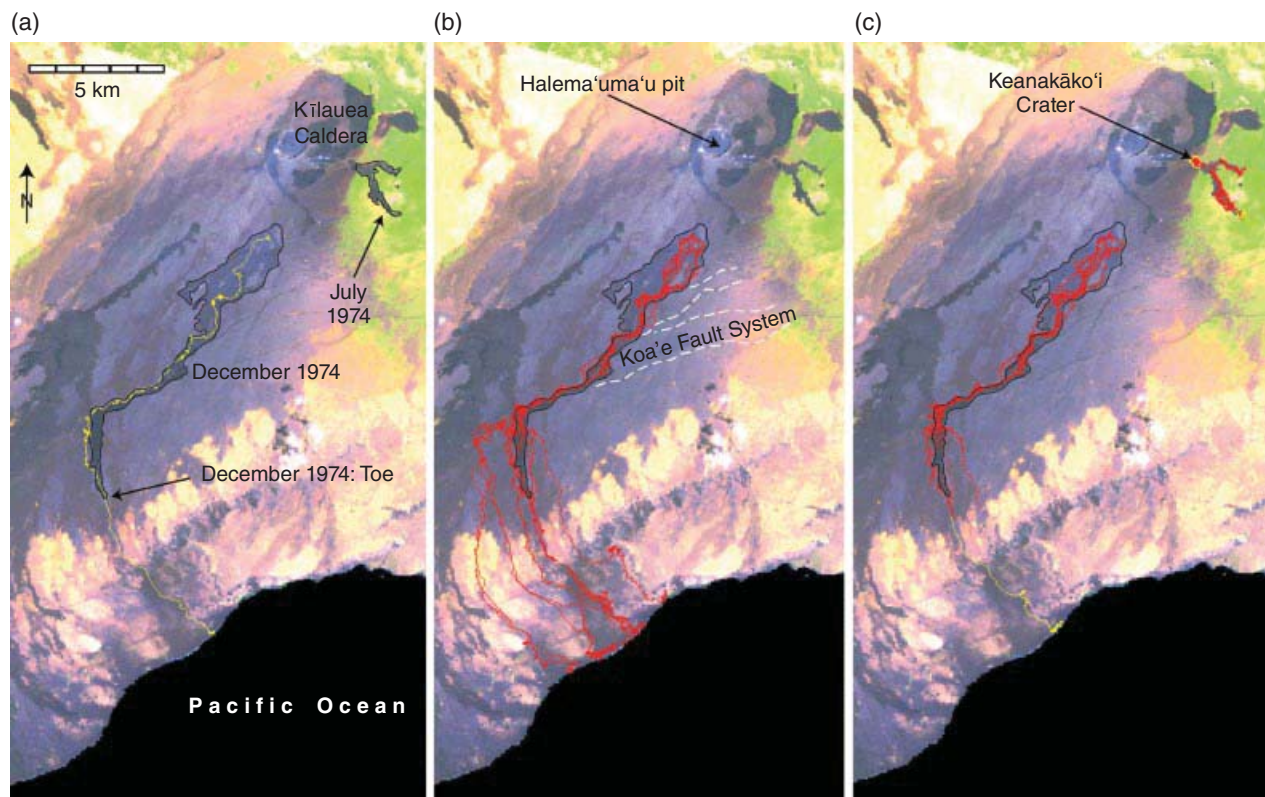


Figure 21.11 FLOWGO-DOWN-FLOW simulation of Kīlauea's July and December 1974 flows whose approximate flow field perimeters are outlined in black, as apparent on the Thematic Mapper color composite underlay. (a) Line of steepest descent from the December 1974 vent zone to the coast (line in yellow). (b) FLOWGO-DOWN-FLOW simulations of the December 1974 flow (red lines, iterations 20, noise 3 m, effusion rate 500 m³/s), with main fault scarps (down throw to NNE) as apparent from shadows in the image marked using dashed white lines. (c) FLOWGO-DOWN-FLOW simulation of the July and December 1974 flows (red lines, iterations 20, noise 3 m, effusion rate 50 m³/s). Modified from Harris [2013].

The line of steepest descent for this flow (Figure 21.11a) follows the flow field center line, without falling off of the topographic “high” caused by the flow field being present in the DEM, as was the case for our Mauna Loa 1984 flow path. This is probably due to the very thin character of this flow field, lava flows being typically less than 1 m thick [Lockwood *et al.*, 1999]. This thickness is less than the 3 m vertical resolution of the DEM, so that the flow is too thin to be properly registered and is thus not apparent in our DEM,

Run iteratively at 500 m³/s, we obtain an array of flow lines all of which reach the ocean, attaining run-outs with an average length of 21.7 km (Figure 21.11b). Flow lines are well concentrated within the actual flow field area over the first ~8 km of flow, following the north – northeast facing fault scarps of the Koa'e Fault System in a south-east direction. Thereafter, flow lines turn south and fan out as they extend directly downslope to the ocean. Over the first 10 km slopes are rather shallow being, on average, 2.15°, thereafter having an average of 5.9°.

Reducing the effusion rate used in the model to 270 m³/s still yields flow lines that attain the coast. However, over the first 10 km of the model run average velocity is 3.3 m/s (5.9 m/s at the vent), and we have a flow interior that cools by 12°C, to give a typical cooling rate of 1.2°C/km. This cooling rate is the same as that calculated by Soule *et al.* [2004] for this flow, and velocities are in line with the 1–6 m/s range estimated for this flow by Lockwood *et al.* [1999] and Soule *et al.* [2004]. To obtain the correct length, we have to reduce the effusion rate used in the model to 50 m³/s (Figure 21.11c). This now gives a channel length of ~10 km and suggests that this flow was volume limited. That is, supply was terminated before the flow had attained its full, potential, cooling-limited extent. This seems consistent with (1) the short duration of the eruption, (2) the fact that the lava interior had only cooled by 10°C after 10 km, and (3) the flow field having only a length of 12 km when effusion rates were at least 270 m³/s. FLOWGO modeling indicates that, had supply to this flow not been cut after 6 h, the channel-fed flow would

have been capable of extending up to 22 km, thereby reaching the coast.

21.6. CONCLUSION

FLOWGO provides a framework within which to review and link thermo-rheological lava properties and relations and produce thermodynamic histories for channel-contained lava control volumes. This aim is best achieved through a best fit with all available field and sample data, and the current version of FLOWGO allows a high degree of manipulation and iteration to allow thermo-rheological and dimensional fitting, as we have done here for some Hawaiian lavas. This model is for an idealized lava flow and uses relatively simple models for cooling, rheology, and flow dynamics. The approach is thus intended to provide useful insights into these phenomena. FLOWGO is not meant to accurately re-create a natural flow. Simulations that allow lava to spread, thicken, and evolve require application of cellular automata models, such as SCIARA (Crisci *et al.*, 2004), MAGFLOW (Del Negro *et al.*, 2008), or LavaSIM (Hidaka *et al.*, 2005). In these models, the thermal and rheological conditions of each pixel across the flow field evolve with time as well as distance from the source (Harris, 2013).

Clearly, the thermal and rheological conditions as well as the associated flow regimes change significantly down a lava channel [e.g., Soule *et al.*, 2004; Woodcock and Harris, 2006; Riker *et al.*, 2009]. This points to a complex flow regime that requires application of an extremely sophisticated and highly flexible model if we are to obtain perfect fits between model output and natural data. To obtain a best fit with all dimensional, dynamic, thermal, and rheological variables, the thermo-rheological conditions as well as the relations themselves may have to be changed down-channel as flow conditions and regimes change. In addition, we need to generate relations that are currently not available. For FLOWGO, the most obvious improvement would be addition of a down-flow vesiculation model that allows the size, shape, and number of vesicles to be calculated at each step as well as a rheological treatment that varies depending on whether Newtonian, Bingham, or viscoelastic conditions are appropriate. For now, the approximations provided by FLOWGO indicate that the relations and input parameters remain reasonable starting points on which we can build.

Our ability to model is limited by our ability to parameterize and link the physics and dynamics behind the phenomena in question. Lava is a challenging fluid to model, and FLOWGO is an attempt to link available knowledge and provide a framework within which we can identify the holes in our understanding.

REFERENCES

- Armienti, P., F. Barberi, F. Innocenti, M. Pompilio, R. Romano, and L. Villari (1984), Compositional variation in the 1983 and other recent Etnean lavas: Insights on the shallow feeding system, *Bull. Volcanol.*, 47(2), 995–1007.
- Armienti, P., R. Clocchiatti, M. D’Orazio, F. Innocenti, R. Petrini, M. Pompilio, S. Tonarini, and L. Villari (1994), The long-standing 1991–1993 Mount Etna eruption: Petrography and geochemistry of lavas, *Acta Vulcanol.*, 4, 15–28.
- Bailey, J. E., A. J. L. Harris, J. Dehn, S. Calvari, and S. K. Rowland (2006), The changing morphology of an open lava channel on Mt. Etna, *Bull. Volcanol.*, 68, 497–515.
- Basaltic Volcanism Study Project (1981) Basaltic Volcanism on the Terrestrial Planets, Pergamon Press, New York.
- Bottinga, Y., and D. F. Weill (1970), Densities of liquid silicate systems calculated from partial molar volumes of oxide components, *Am. J. Sci.*, 269, 169–182.
- Bottinga, Y., and D. F. Weill (1972), The viscosity of magmatic silicate liquids: A model for calculation, *Am. J. Sci.*, 272, 438–475.
- Calvari, S., and H. Pinkerton (1998), Formation of lava tubes and extensive flow field during the 1991–1993 eruption of Mount Etna, *J. Geophys. Res.*, 103(B11), 27,291–27,301.
- Crisci, G. M., S. Di Gregorio, R. Rongo, and W. Spataro (2004), The simulation model SCIARA: The 1991 and 2001 at Mount Etna, *J. Volcanol. Geotherm. Res.*, 132, 253–267.
- Crisp, J., and S. Baloga (1994), Influence of crystallization and entrainment of cooler material on the emplacement of basaltic aa lava flows, *J. Geophys. Res.*, 99(B6), 11,819–11,831.
- Crisp, J., K. V. Cashman, J. A. Bonini, S. B. Houghton, and D. C. Pieri (1994), Crystallization history of the 1984 Mauna Loa lava flow, *J. Geophys. Res.*, 99(B4), 7177–7198.
- Daneš, Z. (1972), Dynamics of lava flows, *J. Geophys. Res.*, 77, 1430–1432.
- Del Negro, C., L. Fortuna, A. Herault, and A. Vicari, (2008), Simulations of the 2004 lava flow at Etna volcano by the mag-flow cellular automata model, *Bull. Volcanol.*, doi:10.1007/s00445-007-0168-8.
- Dragoni, M. (1989), A dynamical model of lava flows cooling by radiation, *Bull. Volcanol.*, 51, 88–95.
- Einstein, A. (1906), Eine neue bestimmung der molekuldimensionen, *Ann. Phys.*, 19, 289–306.
- Fairfield, J., and P. Leymarie (1991), Drainage networks from grid digital elevation models, *Water Resour. Res.*, 27(5), 709–717.
- Favalli, M., M. Pareschi, A. Neri, and I. Isola (2005), Forecasting lava flow paths by a stochastic approach, *Geophys. Res. Lett.*, 32(L03305), 1–17.
- Flynn, L. P. and P. J. Mouginiis-Mark (1994), Temperature measurements of an active lava channel from spectral measurements, Kilauea Volcano, Hawai’i. *Bull. Volcanol.*, 56, 297–301.
- Ganci, G., A. Vicari, A. Cappello, and C. Del Negro (2012), An emergent strategy for volcano hazard assessment: From thermal satellite monitoring to lava flow modeling, *Remote Sens. Environ.*, 119, 197–207.
- Giordano, D., and D. B. Dingwell (2003), Viscosity of hydrous Etna basalt: Implications for Plinian-style basaltic eruptions, *Bull. Volcanol.*, 65, 8–14.

- Giordano, D., A. Mangiacapra, M. Potuzak, J. K. Russell, C. Romano, D. B. Dingwell, and A. Di Muro (2006), An expanded non-Arrhenian model for silicate melt viscosity: A treatment for metaluminous, peraluminous and peralkaline liquids, *Chem. Geol.*, **229**, 42–56.
- Harris, A., J. Bailey, S. Calvari, and J. Dehn (2005), Heat loss measured at a lava channel and its implications for down-channel cooling and rheology, *Geol. Soc. Am. Spec. Pap.*, **396**, pp. 125–146.
- Harris, A., M. Favalli, F. Mazzarini, and M. T. Pareschi (2007), Best-fit results from application of a thermo-rheological model for channelized lava flow to high spatial resolution morphological data, *Geophys. Res. Lett.*, **34**(L01301), doi:10.1029/2006GL028126.
- Harris, A. J. L. (2013), Lava flows, in *Modeling Volcanic Processes: The Physics and Mathematics of Volcanism*, Chapter 5, edited by S. A. Fagents, T. K. P. Gregg, and R. M. C. Lopes, Cambridge University Press, pp. 85–106.
- Harris, A. J. L., and J. S. Allen, III (2008), One-, two- and three-phase viscosity treatments for basaltic lava flows, *J. Geophys. Res.*, **113**, B09212, doi:10.1029/2007JB005035.
- Harris, A. J. L., and S. K. Rowland (2001), FLOWGO: A kinematic thermo-rheological model for lava flowing in a channel, *Bull. Volcanol.*, **63**(1), 20–24.
- Herauld, A., A. Vicari, A. Cirauda, and C. Del Negro (2009), Forecasting lava flow hazards during the 2006 Etna eruption: using the MAGFLOW cellular automata model. *Comp. Geosci.*, **35**, 1050–1060, doi:10.1016/j.cageo.2007.10.008.
- Heslop, S. E., L. Wilson, H. Pinkerton, and J. W. Head III (1989), Dynamics of a confined lava flow on Kilauea volcano, Hawaii. *Bull. Volcanol.*, **51**, 415–432.
- Hess, K.-U., and D. B. Dingwell (1996), Viscosities of hydrous leucogranitic melts: A non-Arrhenian model, *Am. Mineral.*, **81**, 1297–1300.
- Hidaka, M., A. Goto, S. Umino, and E. Fujita (2005), VTFS project: Development of the lava flow simulation code LavaSIM with a model for three-dimensional convection, spreading, and solidification, *Geochem. Geophys. Geosyst.*, **6**, Q07008, doi:10.1029/2004GC000869.
- Hon, K., J. Kauahikaua, R. Denlinger, and K. Mackay (1994), Emplacement and inflation of pahoehoe sheet flows: Observations and measurements of active lava flows on Kilauea Volcano, Hawaii, *Geol. Soc. Am. Bull.*, **106**, 351–370.
- Hulme G. (1974), The interpretation of lava flow morphology, *Geophys. J. R. Astron. Soc.*, **39**, 361–383.
- Ishihara, K., M. Iguchi, and K. Kamo (1990), Numerical simulation of lava flows on some volcanoes in Japan. In *Lava Flows and Domes*, edited by J. Fink, Berlin: Springer, pp. 184–207.
- Jeffreys, H. (1925), The flow of water in an inclined channel of rectangular section, *Philos. Mag.*, **49**, 793–807.
- Jones, R. (2002), Algorithms for using a DEM for mapping catchment areas of stream sediment samples, *Comput. Geosci.*, **28**, 1051–1060.
- Keszthelyi, L. (1995), A preliminary thermal budget for lava tubes on the Earth and planets, *J. Geophys. Res.*, **100**, No.(B10), 20,411–20,420.
- Keszthelyi, L., and S. Self (1998), Some physical requirements for the emplacement of long basaltic lava flows, *J. Geophys. Res.*, **103**(B11), 27,447–27,464.
- Lipman, P. W., and N. G. Banks (1987), Aa flow dynamics, Mauna Loa 1984, U.S. Geol. Surv. Prof. Pap. 1350, pp. 1527–1567.
- Llewellyn, E. W., and M. Manga (2005), Bubble suspension rheology and implications for conduit flow, *J. Volcanol. Geotherm. Res.*, **143**, 205–217.
- Lockwood, J. P., N. G. Banks, T. T. English, L. P. Greenland, D. B. Jackson, D. J. Johnson, R. Y. Koyanagi, K. A. McGee, A. T. Okamura, and J. M. Rhodes (1985), The 1984 eruption of Mauna Loa volcano, Hawaii, *Eos Trans. AGU*, **66**, 169–171.
- Lockwood, J. P., R. I. Tilling, R. T. Holcomb, F. Klein, A. T. Okamura, and D. W. Peterson (1999), Magma migration and resupply during the 1974 summit eruptions of Kilauea volcano, Hawaii, U.S. Geol. Surv. Prof. Pap., 1613, 37 pp.
- Manga, M., J. Castro, K. V. Cashman, and M. Loewenberg (1998), Rheology of bubble-bearing magmas, *J. Volcanol. Geotherm. Res.*, **87**, 15–28.
- Mano, J. F., and E. Pereira (2004), Data analysis with the Vogel-Fulcher-Tammann-Hesse equation, *J. Phys. Chem.*, **108**, 10,824–10,833.
- Mark, D. M. (1984), Automated detection of drainage networks from digital elevation models, *Cartographica*, **21**, 168–178.
- Mazzarini, F., M. T. Pareschi, M. Favalli, I. Isola, S. Tarquini, and E. Boschi (2007), Lava flow identification and aging by means of LiDAR intensity: The Mt. Etna case, *J. Geophys. Res.*, **112**, B02201, doi:10.1029/2005JB004166.
- Moore, H. J. (1987), Preliminary estimates of the rheological properties of 1984 Mauna Loa Lava, U.S. Geol. Surv. Prof. Pap. 1350, pp. 1569–1588.
- O’Callaghan, J. F. and D. M. Mark (1984), The extraction of drainage networks from digital elevation data, *Computer Vision, Graphics and Image Processing*, **28**, 323–344.
- Pal, R. (2003), Rheological behavior of bubble-bearing magmas, *Earth Planet. Sci. Lett.*, **207**, 165–179.
- Park, S., and J. D. Iversen (1984), Dynamics of lava flow: Thickness growth characteristics of steady two-dimensional flow, *Geophys. Res. Lett.*, **11**(7), 641–644.
- Phan-Thien, N., and D. C. Pham (1997), Differential multiphase models for polydispersed suspensions and particulate solids, *J. Non-Newtonian Fluid Mech.*, **72**, 305–318.
- Pinkerton, H., and R. J. Stevenson (1992), Methods of determining the rheological properties of magmas at sub-liquidus temperatures, *J. Volcanol. Geotherm. Res.*, **53**, 47–66.
- Rhodes, J. M. (1988), Geochemistry of the 1984 Mauna Loa eruption: Implications for magma storage and supply, *J. Geophys. Res.*, **93**(B5), 4453–4466.
- Riker, J. M., K. V. Cashman, J. P. Kauahikaua, and C. M. Montierth (2009), The length of channelized lava flows: Insight from the 1859 eruption of Mauna Loa volcano, Hawai’i, *J. Volcanol. Geotherm. Res.*, **183**, 139–156.
- Roscoe, R. (1952), The viscosity of suspensions of rigid spheres, *Br. J. Appl. Phys.*, **3**, 267–269.
- Rowland, S. K., A. J. L. Harris, and H. Garbeil (2004), Effects of Martian conditions on numerically modeled, cooling-limited, channelized lava flows, *J. Geophys. Res.*, **109**, E10010, doi: 10.1029/2004JE002288, 1–16.
- Rowland, S., H. Garbeil, and A. Harris (2005), Lengths and hazards from channel-fed lava flows on Mauna Loa, Hawai’i, determined from thermal and downslope modeling with FLOWGO, *Bull. Volcanol.*, **67**, 634–647.

- Shaw, H. R. (1969), Rheology of basalt in the melting range, *J. Petrol.*, 10(3), 510–535.
- Shaw, H. R. (1972), Viscosities of magmatic silicate liquids: an empirical method of prediction, *Am. J. Sci.*, 272, 870–893.
- Soule, S. A., K. V. Cashman, and J. P. Kauahikaua (2004), Examining flow emplacement through the surface morphology of three rapidly emplaced, solidified lava flows, Kilauea volcano, Hawai'i, *Bull. Volcanol.*, 66, 1–14.
- Tanguy, J. C. (1973), The 1971 Etna eruption: Petrology of the lavas, *Philos. Trans. R. Soc. Lond.*, 274, 45–53.
- Thorner, C. R. (2001), Olivine-liquid relations of lava erupted by Kilauea volcano from 1984 to 1998: Implications for shallow magmatic processes associated with the ongoing east-rift-zone eruption, *Can. Mineral.*, 39, 239–266.
- Tonarini, S., P. Armienti, M. D'Orazio, F. Innocenti, M. Pompilio, and R. Petrini (1995), Geochemical and isotopic monitoring of Mt. Etna 1989/1993 eruptive activity: Bearing on the shallow feeding system, *J. Volcanol. Geotherm. Res.*, 64, 95–115.
- Turcotte, R., Fortin, J.-P., Rousseau, A. N., Massicotte, S. and J.-P. Villeneuve (2001), Determination of the drainage structure of a watershed using a digital elevation model and a digital river and lake network, *J. Hydrol.*, 240, 225–242.
- Vicari, A., A. Herault, C. del Negro, M. Coltelli, M. Marsella, and C. Proietti (2007), Modeling of the 2001 lava flow at Etna volcano by a Cellular Automata approach, *Environmental Modelling and Software*, 22, 1464–1471.
- Vicari, A., A. Cirauco, C. del Negro, A. Herault, and L. Fortuna (2009), Lava flow simulations using discharge rates from thermal infrared satellite imagery during the 2006 Etna eruption, *Natural Hazards*, 50, 539–550.
- Vicari, A., G. Ganci, B. Behncke, A. Cappello, M. Neri, and C. del Negro (2011), Near-real-time forecasting of lava flow hazards during the 12–13 January 2011 Etna eruption, *Geophys. Res. Lett.*, 38, L13317, doi: 10.1029/2011GL047545.
- Whittington, A., P. Richet, Y. Linard, and F. Holtz (2001), The viscosity of hydrous phonolites and trachytes, *Chem. Geol.*, 174, 209–223.
- Wilson, M. (1989), *Igneous Petrology: A Global Tectonic Approach*, Unwin Hyman, London, 466 pp.
- Woodcock, D., and A. Harris (2006), The dynamics of a channel-fed lava flow on Pico Partido volcano, Lanzarote, *Bull. Volcanol.*, 69, 207–215.
- Wooster, M., R. Wright, S. Blake, and D. Rothery (1997), Cooling mechanisms and an approximate thermal budget for the 1991–1993 Mount Etna eruption, *Geophys. Res. Lett.*, 24(24), 3277–3280.
- Wright, R., H. Garbeil, and A. J. L. Harris (2008), Using infrared satellite data to drive a thermo-rheological/stochastic lava flow emplacement model: A method for near-real-time volcanic hazard assessment, *Geophys. Res. Lett.*, 35, L19307, doi:10.1029/2008GL035228.
- Young, P. and G. Wadge (1990), FLOWFRONT: Simulation of a lava flow, *Comp. Geosci.*, 16, 1171–1191.
- Zhang, Y., Z. Xu, and Y. Liu (2003), Viscosity of hydrous rhyolitic melts inferred from kinetic experiments, and a new viscosity model, *Am. Mineral.*, 88, 1741–1752.